Master's thesis

Oskar Perstølen

Electron transport and characterization of semiconductor/superconductor nanowires

UNIVERSITY OF COPENHAGEN

Date: July 16, 2022

Advisor: Jesper Nygård

Abstract

This thesis explores the properties of bandgap engineered $InAs/InAs_{1-x}Sb_x$ type nanowires for in-situ growth of axial quantum dots. The careful control of crystal phase when adding antimony allows us to grow short segments of wurtzite (InAs) incorporated into a zincblende ($InAs_{1-x}Sb_x$) nanowire. The heterostructured nanowires have been characterized with electron microscopes, and devices were made for electron transport measurements. Different growth parameters such as temperature, precursor diameter and V/III flux ratio allow us to optimize for later application. Dark field mode in transmission electron microscope was used to determine the dimensions of the quantum dot. The best conditions for stable long range coulomb resonances were found to be in QD with lower diameter grown at 433^oC.

In the second part of this thesis, you will read about quantum transport measurements on InAs double nanowires with a superconducting lead island bridging the wires together. From transport measurements we have understood the device to consist of three strongly coupled contacts and one weakly coupled through a N-QD-S junction. The behavior of the island was investigated in magnetic field and temperature, which suggest we have quasi-particle poisoning from one of the strongly coupled leads. We extracted the effective g factor of a subgap state which could be tuned with the coupling of the weakly coupled contact.

Preface

When I came to Denmark for my master thesis I knew one thing; my path is nanophysics, and quantum mechanics is cool. I had no relationship to nanowires, and superconductivity was something magical. I was lucky enough to have a fellow student recommend qdev, and I am so very lucky that there was room for me. I have really enjoyed the work that I have done this last year, but none of it would have been the same without the people around me. I will start off to thank Christian Petersen for tipping me off about looking for master project at qdev, and for being one of my best friends after arriving in Denmark. Daniel Ross who were there early to integrate me into the group. Daniel Kjær which I have had the pleasure to work alongside in parallel this whole time. James Xu whose projects are always interesting to hear more about. Joachim Sestof who is never afraid of sharing a good laugh. I am also very impressed with your patience while helping me out early on with every fabrication step, and always being available in times of crisis or for any discussion. Alexandros Vekris who's expertise on double nanowires island devices were of immense help. Juan Carlos with his vast knowledge of quantum transport measurement's. Xiangyu Lin who have been my partner in measurement these last couple of months. Rasmus Schlosser, for all the good discussions on everything. Thomas Kanne for helping me out in every step during my Master thesis. From proposing project, to discussing results. I also appreciate the opportunity you gave me to experience the MBE system, and be apart of the discussion around what to grow. Kasper Grove Rasmussen for he's ability to answer any question I could come up with, and for helping out when there were any trouble with a fridge. And of course Jesper Nygård for giving me the opportunity to be a part of his fantastic group, and for giving me the independence and trust to work on what I believe (and know) is some very expensive equipment. Thanks again to all for making my time here be everything I could have hoped for.

Table of content

List of abbreviations

MBE - Molecular Beam Epitaxy

QD - Quantum dot

SEM - Scanning electron microscope

SE - Secondary electrons

BSE - Backscattered electrons

TEM - Transmission electron microscope

SAED - Selected area electron diffraction

VLS - Vapor Liquid Solid

ZB - Zincblende

WZ - Wurtzite

PVD - Physical vapor deposition

DAC - Digital to analog converter

AC - Alternating current

DC - Direct current

DMM - Digital multimeter

MZM - Majorana Zero Mode

BCS - Bardeen Cooper Schrieffer

ABS - Andreev Bound state

1   Introduction

Nanotechnology has over the last couple of decades become one of the most exciting areas of research, with applications in everything from batteries [1] to drug delivery systems [2]. The exciting phenomenon's that emerges when special dimensions are limited to the nano scale is the driving force behind this. One field that falls under the nanotechnology umbrella is research into semiconducting materials at the nano scales, and in our case binary and ternary III – V semiconducting nanowires.

Semiconducting nanowires have shown promise for future application in electronics [3], photonics [4], thermoelectric [5], and more. Nanowires are quasi-1-dimensional objects with diameter ranging around 100 nm, where the confined cross section allows for quantization of energy levels of the transverse modes[6]. The low charge carrier density of semiconductors make them ideal materials for manipulation of electron states by gating. If a superconducting metal is put in proximity to a nanowire, the superconducting phase will penetrate into the semiconductor and a hybrid states can emerge which contain properties from the semiconductor and the superconductor.

One III - V semiconducting NW which has gained lots of attention is the InAs. InAs possess a low electron effective mass, strong spin – orbit interaction and high carrier mobility [7]. All of these contributes have made InAs a host for hybrid semiconductor/superconductor nanowire systems for research into topological qubits in quantum computing[8]. The ternary compound $InAs_{1-x}Sb_x$ have been shown to exhibit even greater spin orbit coupling [9] which could be of interest for future hybrid devices.

What is of most interest for much of the work presented in this theses is Band gap mismatch between InAs and $InAs_{1-x}Sb_x$ which we intend to exploit for as grown axial quantum dots. As grown quantum dots (QD) can be implemented into existing research on hybrid nanowire devices where previous studies have relied on gate induced QD's [10][11], where an as grown QD will give better control. One device in particular is a cooper pair splitter, where a superconducting lead is coupled to two QD's, one on each wire in a double wire setup[12]. This will talked more about in the final chapter. The focus of the work presented here is to explore growth parameters as we chase a stable and reproducible as grown QD.

1.1 Outline

The thesis will start off in chapter two with introducing the two electron microscopes and their relevant modes. The theory regarding the InAs/InAsSb nanowire growth and the tool box required for describing electron transport across a quantum dot will also be covered. The fabrication steps and measurement setup will be introduced in chapter three. In chapter four, transport data and characterization of the InAs/InAsSb nanowires will be discussed. Chapter 5 will take a detour and cover the measurements we did on a double nanowire bridged together with a superconducting Pb island device. The final chapter will include a conclusion together with an outlook.

2 Theory

In this chapter most of the background required for further discussion later on heterostructured InAs/InAsSb wires will be presented. First out is an introduction to nanowire growth and the careful control of the crystal phase, which is followed by how to engineer the band gap of InAsSb wires. This section will conclude with electron transport across a quantum dot, with the capacitance model for support, and how to read off the plots that will be presented later.

2.1 Characterization of nano materials

2.1.1 Scanning Electron Microscope

On of the most popular characterization technique used for nano materials is the scanning electron microscope (SEM). The keyword here is nano. Optical microscopes resolution limit is given by eq.1(adopted from ref.[13]), which tells us that the resolution limit of an optical microscope is about half its wavelength, λ.

$$R = \frac{0.61\lambda}{\mu sin(\phi)} \tag{1}$$

Considering the visible spectrum is between 400 and 800 nm, an obvious problem emerges. There are ways to go below which involves using different mediums with larger diffraction index (μ), or changing the angle of the cone of light from the source to the objective lens (ϕ), but a hard limit is at 200 nm, which is too big for our work. The other option is to use a different source to "light up" the sample. That takes us back to the SEM.

There are plenty of signal sources to pick from when taking an SEM image, but the three most popular are the secondary electrons (SE), back scattered electrons (BSE), and characteristic x-rays, as shows in fig.1. The typical energy used in the SEM are acceleration voltages between 0.1 and 30 kV. Characteristic x-rays are used for an element analysis of the sample. The SE are low energy electrons knocked out by an inelastic collision between primary beam electrons and the electrons in the sample. The loss in energy causes the interaction zone to be smaller and this source will for the most part image the surface of the sample. Note that the interaction zone only talks about electrons that escape the sample. There are plenty of SE along
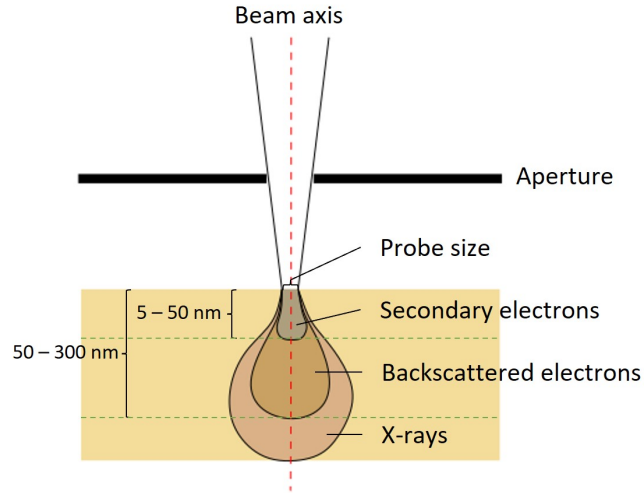
Figure 1: Illustration of interactions zone for an electron beam after contact with a surface. Note that if the sample is sufficiently thin the electrons will transmit through.

the entire beam path. SE are by far the most used mode in house because of its easy and quick use. BSE are high energy primary beam electrons that elastically are "bounced" back by the sample. The high energy allows for much deeper penetration of the sample and still being able to escape. The unique feature of the BSE is that they are to a greater degree element specific. Higher atomic numbers will generate more BSE due to the more electron dense nature, and will show as brighter on the monitor. What's common for both is that the resolution is limited by the probe size and interaction zone.[13]

With electron microscope we cant use the wavelength of electrons alone to give an approximate resolution limit as we do with the optical microscope. If that were the case we would have a resolution of single digit Ångstrøm with an acceleration voltage of 10 kV. That is simply not the case, and we must consider spherical aberration. There are however two opposites that fight for resolution limits. The probe size can be calculated from eq.2 which is take from ([13]).

$$d_{min} = KC_s^{1/4}\left(\frac{i_p}{\beta} + \lambda^2\right)^{3/8} \tag{2}$$

Here we neglect the chromatic aberration and assume it is perfect, hence the notation d_{min}. It is obvious that to minimize the probe size we need to limit spherical

aberration (C_s) and the electron wavelength (λ), and we should maximize the brightness ($\beta \propto eV_0$) where V_0 is the acceleration voltage. The brightness also depends on electron source. The last variable to mention is i_p which is the probe current. From this equation alone it seems like higher acceleration voltage solves all our problems, but that is sadly not true. Resolution doesn't only depend on the probe size, but also the interaction zone as shown in fig.1. Higher electron energy will interact more in the sample. It is therefore important to also have a good electron source which can maximize β without increasing the energy for optimal resolution. Another issue with increased acceleration voltage is damage to the sample. From fig.1 it's clear that the resolution of SE is better than that of the BSE. This is the case for equal energy, but generally you would use a smaller acceleration voltage with the BSE. The in house SEM we use is a JEOL 7800F field emission SEM, and with an acceleration voltage of 10 kV has a probe size of around 2 - 3 nm, but we can assume the real resolution is a bit worse than this. Luckily this is enough for fabrication of nano devices, but if we want to take a closer look at our samples for characterization purposes we need to do better.

2.1.2 Transmission Electron Microscope

Transmission Electron Microscope (TEM) is an imaging technique where we look at electrons that pass through a sample. The most popular mode involves illuminating the whole sample with electrons, but it is also possible to scan the sample like we do in the SEM. A typical acceleration voltage is 200kV.

One requirement for the TEM is that the specimen under investigation is thin enough for sufficient electron transparency. There is no single answer to this, and the value differ between elements like how the BSE imaging in SEM get elemental contrast. However, a rule of thumb would be to stay below 100 nm when you can. Luckily for us our nanowires are between 80 and 250 nm in diameter and can be imaged as is without any sample preparation[14].

The sample is position on a TEM grid which consist of a grid pattern of copper with holes. The holes are covered in a carbon thin film which allow for easy transmission of electrons, and it's on this thin film the wires are positioned. The transfers of wires from the growth substrate to the TEM grid can be done at random where the TEM grid is pushed into the nanowires, and some of the wires will break and

stick to the grid. The more controllable way of doing it is to transfer the wires using the micro manipulator, which is discussed later. We generally transferred wires to keep track of which wires we were looking at [14].

A TEM image is created from electrons scattering off the sample, and what we see on the detector are the transmitted and refracted electrons. When a wave of a single electrons hit a crystalline sample. Certain angles of diffraction will result in constructive interference of the exiting electron wave at the same angle. When two planes (or more) in a crystal lies parallel they have the same set of miller indices (hkl). An incoming wave of electrons that hit the one set of planes at an angle will diffract. Since we are coming at an angle the electron wave will naturally travel further to reach to planes in the back. If the angle of the incident beam fulfills the Bragg condition, the wave diffraction off different planes will have traveled a difference in length which is exactly and integer of the wavelength[14].

$$2dsin(\theta_B) = n\lambda \tag{3}$$

Eq.3 is the condition required for constructive interference of the diffracted electron wave. This is also illustrated on the left in fig.2, where the incident beam (red) hits the planes at an angle (θ_B) such that the extra distance covered ($2dsin(\theta_B)$) is exactly an integer number of the wavelength, λ. This is illustrated with the two waves exciting the crystal being two wavelengths out of phase. d is the lattice plane spacing.

Each set of planes will have a Bragg angle corresponding to the constructive interference off the plane. When these are put together, a plane with diffraction peaks in a pattern will emerge in the reciprocal space. This pattern is the Selected Area Electron Diffraction (SAED) pattern, and each diffraction peak can be labeled with a set of miller indices. What is fantastic about the SAED pattern is that each peak only contains generally one or only a few planes. By putting an aperture over a selected peak, and blocking out all the other, an image with the selected crystal plane lights up while all else is dark. The is the dark field view. Selecting specific crystal planes becomes a great tool for separating different crystal phases in a polycrystalline material[14].

In a thick enough sample large number of electrons will incoherently scatter in all direction. The number of scattered electrons is important to get a good enough
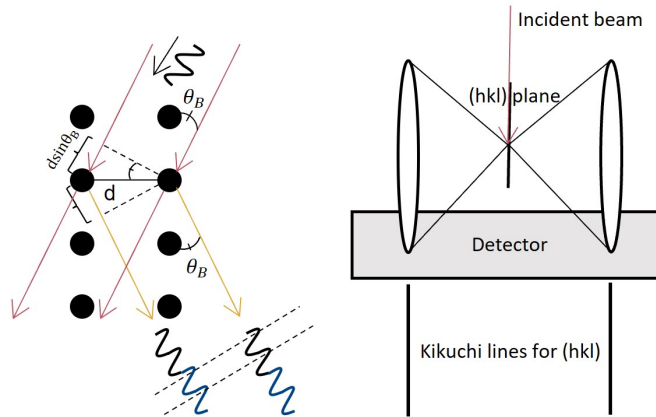
Figure 2: On the left diffraction of the incoming electron beam leading to diffraction peaks. On the left are incoherent scattering in a lattice plane with miller indices (hkl), and the resulting Kikuchi lines.

signal. As they scatter in all directions two cones extend in opposite direction of each other from a plane in the lattice, which is illustrated on the right in fig.2. This is because the incident beam does not come from a single incident k-vector, but rather a range of k-vectors. When the cones and the detector intersect, two lines, one for each cone, will be visible. Each lattice plane in the crystal will have a corresponding diffraction peak, and a pair of Kikuchi lines[14].

The Kikuchi lines works as a map for orienting the crystal. How to think about it is that if a pair of Kikuchi lines are at the center of the detector, the corresponding plane is parallel to the incident beam. Finding a region in reciprocal space where multiple Kikuchi lines cross corresponds to an orientation where multiple planes are parallel to the incident beam, and such a high symmetry orientation makes it easier to make a SAED pattern later[14].

2.2 Material science

2.2.1 Vapor liquid solid

All the work presented in this thesis paper were done on nano-wires grown in a Molecular Beam Epitaxy (MBE) system with a bottom up approach. All wires were grown by Thomas Kanne. The wires were made using a growth mode called vapor-

liquid-solid (VLS) [6]. A precursor gold droplet is used as a catalyst to induce a single atomic layer by layer growth of III-V semiconductor on a InAs[111] substrate. The term vapor comes from an atomic beam "vaporized" onto the gold from a source crucible. The atoms are absorbed by the liquid gold catalyst until reaching a supersaturated state. At that point the liquid will solidify, but due to the growth substrate surface lattice symmetry, the most energetically favorable thing to do is for the liquid to make a solid single atomic thick layer on the surface, and from the second layer and onward an atomic layer on the previous layer. The growth rate and diameter of the nano-wires depends on precursor size, temperature, total flux, V/III flux ratio and distance from the gold droplet to the substrate. The last one is due to movement of atoms on the surface of the substrate and the wire. There are two sources of atoms to our liquid droplet. One are direct atoms from the source, but there are also atoms moving around looking for the most energetically favorable place to sit. These are termed adatoms [15], and each element comes with a diffusion length which depends on temperature. From this we can understand that the later stages of the growth where the gold droplet is the furthest away from the substrate, less adatoms will reach the droplet. For reference, the adatom diffusion length of In is about 3μm, and the wires used from device fabrication were up to 10μm.

2.2.2 Crystal structures

InAs will crystallize in a stable Zinc-blende (ZB) phase while in the bulk, but will go in a meta stable wurtzite (WZ) phase as a nanowire. WZ follows a hexagonal ABAB... stacking of planes in the growth direction [0001](see fig.3). A and B refers to a pair of In and As layer, and it follows that the WZ phase is periodic for every second pair of layers. Changes in this order (ie. ABABBA...) will cause stacking faults, which function as scattering sites in the nanowire, and can be problematic during electron transport. The ternary $InAs_{1-x}Sb_x$ compound, where x is the molar fraction of Sb, will have a ZB phase for x > 0.03 in nanowires[16]. The ZB is a cubic crystal which follows an ABCABC... stacking and grows along the [111] direction(see fig.3). ZB is periodic after every third layer. There are two crystal orientations for the ZB phase which are oriented 60 degrees off each other and are called twinnings [17]. The twinning occurs at a single atomic plane, and both orientations match such that the cubic lattice can fulfill all its bonds. The energy needed for a twinning
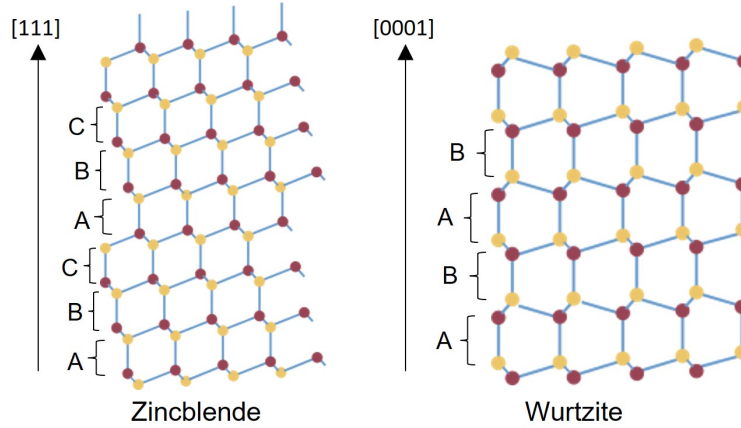
9

Figure 3: The lattice plane stacking of zincblende and wurtzite crystal phase. Red and yellow are the III and V element.

is so low that it can happen at any time during even the best growth conditions. In [18] they found that for x = 0.10 the Sb concentration goes down in the twin boundary which can functions as a scattering site similar to the ones found in WZ. In our work twin planes have generally been less prevalent in ZB phase than stacking faults are in the WZ phase.

In the TEM it is possible to use the SAED mode to isolate the diffracted electron beam intensities between the two crystal phases. This can be done using the objective aperture to isolate the blue diffraction peak seen in fig.4b, and the result can be seen in fig.4a. The brighter areas are due to electrons diffracting off a wurtzite plane in the crystal. This will be further discussed in chapter 4.

2.3   Bandgap engineering

The effect of crystal phase in an InAs NW is that the conduction and valance band of the WZ phase lies above the ZB phase such that there is a type II band alignment [19] [20]. By incorporating a section of WZ in between two sections of ZB creates an energy barrier in the conduction band. Two such barriers following each other will confine an area in all three spatial coordinates and function as a QD.

Crystal phase can be controlled by changing the V/III flux ratios of In and As [21], temperature and diameter [22], while we do it by changing the molar fraction of
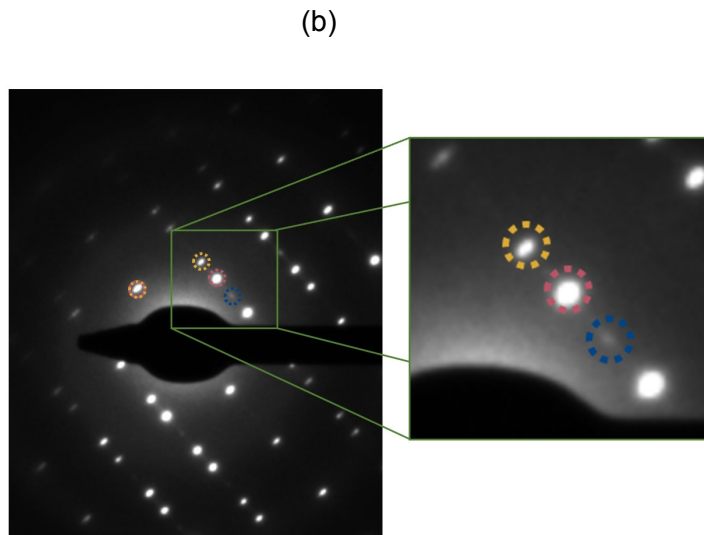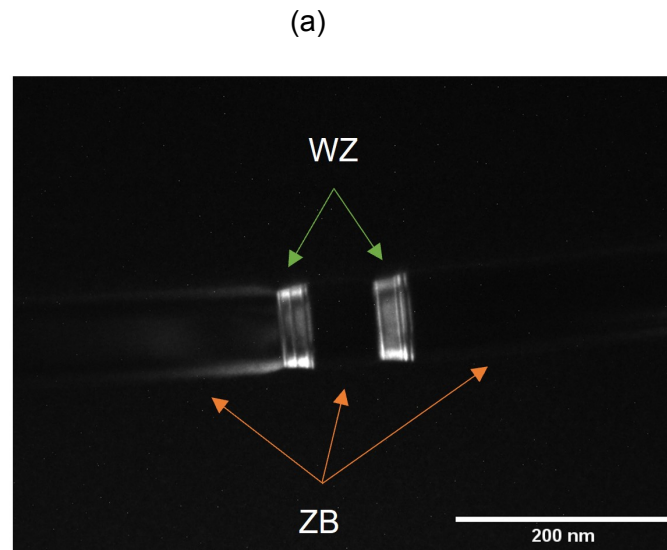
(a)

(b)

Figure 4: a) Selected area diffraction of the wurtzite crystal phase in a nanowire. b) The diffraction pattern. Blue circle is a diffraction peak from the wurtzite, while the yellow and red are the peaks from the two twinning. Note that they overlap in some cases marked with a combination of red and yellow. The diffraction pattern in b) does not belong to the SAD seen in a), but it represent what every diffraction pattern looks like.

Sb. By drawing a line between the two parents of the ternary compounds a bandgap which depends on x allows for engineering of the bandgap. This line connecting the parents can be linear or curved, and in our case the band gap of InAs (ZB) and

InSb (ZB) is related with a curved line. The band gap of $InAs_{1-x}Sb_x$ is calculated in eq.4.

$$E_g^{InAs_{1-x}Sb_x} = E_g^{InSb}x + E_g^{InAs}(1-x) - C_g x(1-x) \tag{4}$$

Here E_g is the band gap $E_{CB}-E_{VB}$, where CB and VB are the conduction band and valence band. C_g is the bowing parameter which also is the difference between the conduction and valance bowing parameter ($C_{CB}-C_{VB}$). The bowing parameter is somewhere on the order of $0.6-1$ eV, and with an E_{VB} offset of 500 meV between InAs and InSb the conduction band of $InAs_{1-x}Sb_x$ can be estimated to have a minima around 0.3 x, which is also where the greatest height of the WZ barrier should be found.
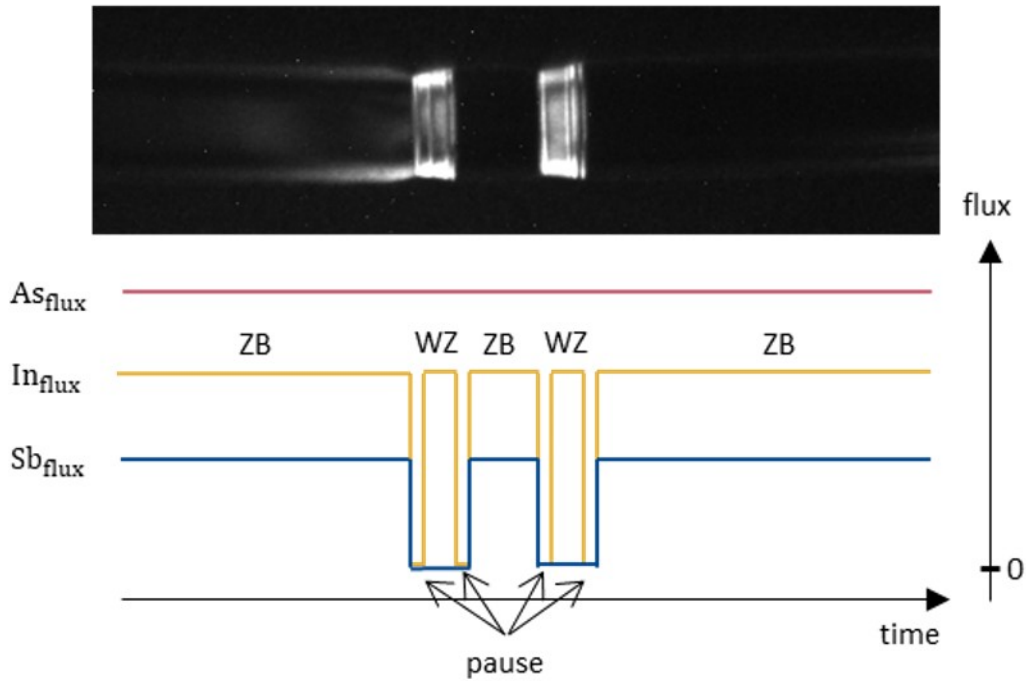

Figure 5: The flux of In, As and Sb over a quantum dot.

During the VLS growth cycle an $InAs_{1-x}Sb_x$ ZB wire is grown with pure InAs WZ barriers, and the growth steps along a single QD is illustrated in fig.5. While transferring from ZB to WZ a pause of In and Sb influx is done to deplete the gold droplet of Sb. Ideally, we want an atomically sharp transition from pure ZB to pure

12

WZ. During the WZ growth only In and As flux is active before a new pause in the next transfer from WZ to ZB growth. This procedure is repeated for every barrier with different growth time for barrier and dot lengths.

2.4 Electron transport

2.4.1 Quantum dots

Quantum dots are quasi atoms where the spacial volume is sufficiently limited such that the otherwise continuous energy spectrum in a solid becomes discrete. They are zero dimensional objects, or as the name suggest, a single dot, compared to it's bulk counterpart. However, in the quantum would the three dimensional size of the dot matters. There are multiple ways for QD's to be engineered, which includes small nano particles [23], regions defined by the split - gate technique [24], confined segments in single nanowires and more, but the principle is the same, the QD's are weakly coupled to its environment such that electron transport into and out of the quantum dot is in the tunneling regime, and the energy specter is discrete[6].

An important effect seen in QD's is the coulomb-blockade, which is a result of electron-electron repulsion and the Pauli principle, which only allows each quantum state to be occupied by a single electron. In a continuous spectrum of electronic states this wont matter much, but when the states becomes discrete this effect becomes increasingly obvious. Lets show this in figure.6a where we have a quantum dot which is confined inside a nanowire (red) by two potential barriers (blue), and two electrodes (gold) are hooked up on each end such that we can send electrons through, but lets keep the bias at zero for now. There needs to be available energy states at each point along the wire for the electrons to move, including the quantum dot. This means we need an available state on the dot for an electron to move through it. Lets turn on the bias a tiny bit, but a lot less then the energy spacing between each discrete electron state. We can now have two situations. There are no available electron states inside the bias window, and this is illustrated in figure.6d. In this case no electrons can jump out of or into the QD. We will have no current through the wire, and this is called the coulomb blockade regime. Effectively the electrons on the dot itself is blocking us from adding an additional electron, and because the drain has higher energy then the highest occupied energy level, no electrons are leaving the QD.
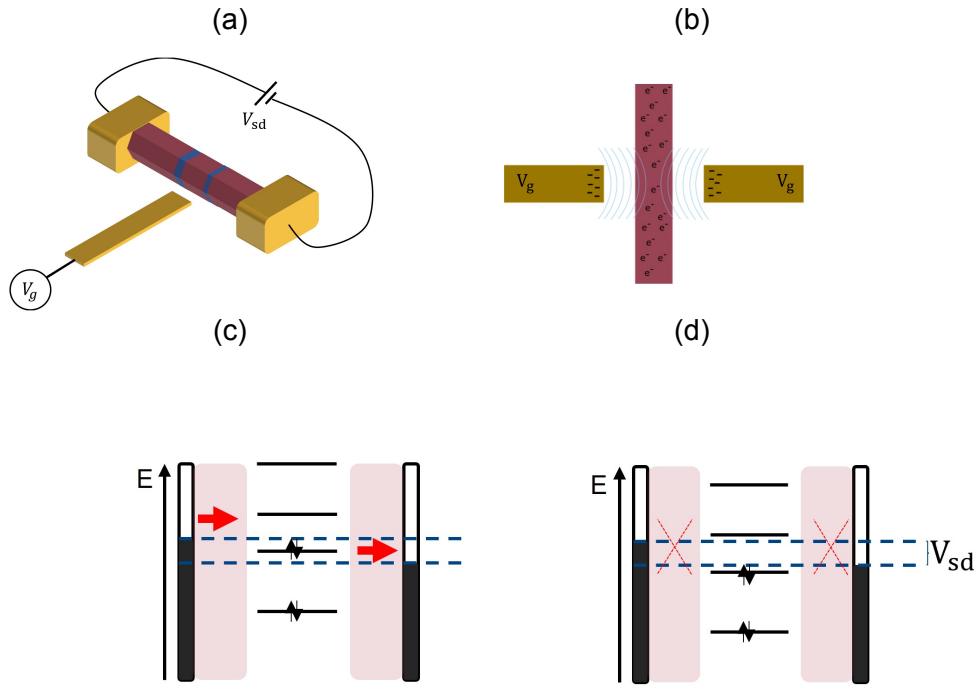
Figure 6: a) Illustration of a quantum dot in a nanowire (red). The potential barriers are shown in blue. The two golden contacts on each side are the source and drain, while the block in front of the QD represent the side gate. b) An illustration of how applying a negative charge on gates will change the energy landscape for electrons inside a nearby nanowire. c) Energy diagrams while in the coulomb resonance regime. d) Energy diagram while in the coulomb blockade regime.

The other situation will be when we do have an electron state inside the bias window such that electrons can move off and on, which is illustrated in fig.6c, and we call this conductance resonance. In this case our drain have available states below the highest occupied state on the dot, and electrons can tunnel out as drawn with a red arrow. This leaves room for a new electron to enter the QD for the source.

Lets return to the gate electrode seen in figure.6a, which in our case is a side gate. There are however different options for a gate electrode. We have top gate, side gate and back gate, but they all function the same way but from different direction. The gate electrode is capacitively coupled to the island and when charging it an electric field changes the electronic states inside the QD, which is illustrated in fig.6b. In order to effectively gate a nanowire you need a low enough charge carrier density
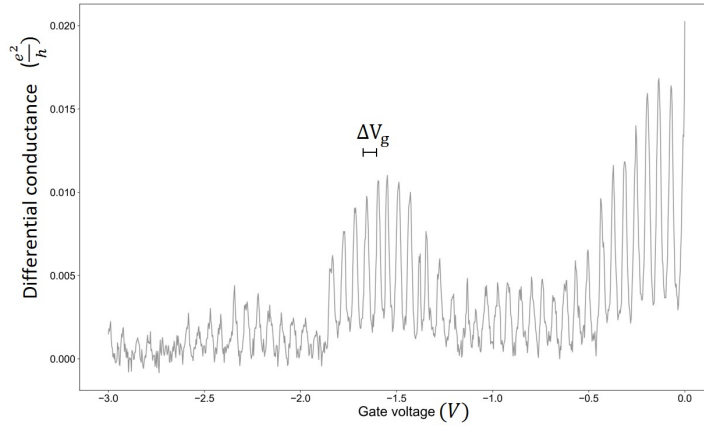
Figure 7: Coulomb resonances by sweeping the gate electrode while keeping the bias voltage at zero.

to begin with. This is why nanowires are not metallic, but rather made out of semiconductors. Gating is done by charging the gate electrode with a positive or negative potential. When a positive charge is put on the gate the resulting electric field lowers the energy of the electronic states in the QD, and the opposite happens when a negative charge is put on it. We can in this way control the electronic configuration on the QD, effectively choose if we want to be on or off resonance.

If we keep the bias window at zero and only sweep the gate electrode we will get periodic coulomb resonances as we see in fig.7. What each peak represent is a state moving across the zero bias window. We do however get the differential conductance even with zero bias because of the AC component.

A requirement for coulomb blockade to arise is that the coulomb energy dominates over all the other energy scales. The main antagonist in that case is temperature, where the requirement is that the charging energy need to be much greater than the thermal energy, i.e eq.5:

$$k_B T << \frac{e^2}{C_\Sigma} \tag{5}$$

There are two ways to work around this, either cool things down a lot, or make smaller quantum dots. The second is due to the capacitance being size dependent, and for big enough QD's cooling down wont do. Another requirement is that the

15

source and drain coupling to the QD is in the tunneling regime. This has to do with Heisenberg's uncertainty relation. Taking the charging energy to be e^2/C_Σ and time it takes to charge an island to be $\Delta t = R_t C_\Sigma$, we get eq.6 for the tunneling resistance R_t.

$$\Delta E_c \Delta t > h$$
$$R_t > \frac{h}{e^2} \tag{6}$$

Here we see that the tunneling resistance must be greater than the resistance quantum, hence the tunneling regime. Another effect to mention is the source for broadening of the resonance levels, which can be either thermally broadened or broadened due to the tunneling coupling, depending on which is greater.

The reason for coulomb blockade, as mentioned, comes from electron electron repulsion and the Pauli principle, but depending on the relative strength of each repulsion the QD can be in two different regimes. In individual atoms we have orbitals with energy states where only a single electron can occupy a set of quantum numbers, and the next electron in line will have to occupy the next set of quantum numbers which could have higher energy. The same can be said about the quantum dot, which functions as an atom in a way. The size of the quantum dot makes the spacing between individual quantum levels change proportionally to $1/r^2$, where r has to do with the size of the QD. This is the Pauli contribution. The electron electron repulsion revolves with the inverse of the radius in first order. The total energy for adding an electron to a QD is the addition energy (E_{add}) which is the sum of both (eq.24

$$E_{add}(N) = E_c + \Delta E(N) \tag{7}$$

For a QD, the quantum confinement will vanish faster with increasing r. This implies that the addition energy for larger QD will stay close to constant if the quantum confinement is negligible, and the charging energy(E_c) will dominate. This can be seen while doing measurements that the diamonds plots, which are introduced in the next sub chapter, have all close to equal height. In the region for smaller r, where the quantum confinement matters ($\Delta E(N)$), the diamonds will alternate in height between odd and even state. The even state will have an increase in E_{add} due to the confinement, while the odd diamond will have the height corresponding

to only E_c due to degeneracy of spin states. In our nanowires this can be controlled by confining the QD in the lateral direction, and if its small enough the QD can even be depleted for states in its natural state[25].

2.4.2 Coulomb Diamond

The coulomb diamonds gets its name from the diamond in a deck of cards, and comes out naturally when source - drain sweep from $\pm E_{add}^{max}$ in steps of the gate electrode. From the diamonds it is possible to extract the addition energy from the height of the diamond, and the lever arm of the gate from the peak spacing at zero bias. If we are in the regime where we can ignore the quantum confinement, we can find the total capacitance from eq.8 where E_c is the height of the diamond times the elemental charge e.

$$E_C = \frac{e^2}{C_\Sigma} \tag{8}$$

We can also find the gate capacitance from the zero bias peak spacing where $\Delta V_g = e/C_g$. Considering that the total capacitance is the sum of all, ie. $C = C_g + C_s + C_d$, and assuming symmetrical coupling to the source and drain, we can find the capacitance of the tunnel coupling from eq.9

$$\begin{aligned} C &= \frac{e^2}{E_c} = C_g + 2C_{sd} \\ C_{sd} &= \frac{e^2}{2E_c} - \frac{C_g}{2} \end{aligned} \tag{9}$$

We can also estimate the tunnel barrier to be a disk with the capacitance: $C_t = \epsilon_r \epsilon_0 A/t$. A is the area of the disk, t is the thickness of the tunneling barrier, ϵ_r is the dielectric constant of the tunnel barrier, and ϵ_0 is the vacuum permittivity[26].

2.4.3 Capacitance model

This can be described more in detail using the capacitance model. In this model the interaction between electrons a represented by a capacitance matrix, C_{ij}, and the charge on any object in the system can be expressed as eq.10 where $Q_i^{(0)}$ is the
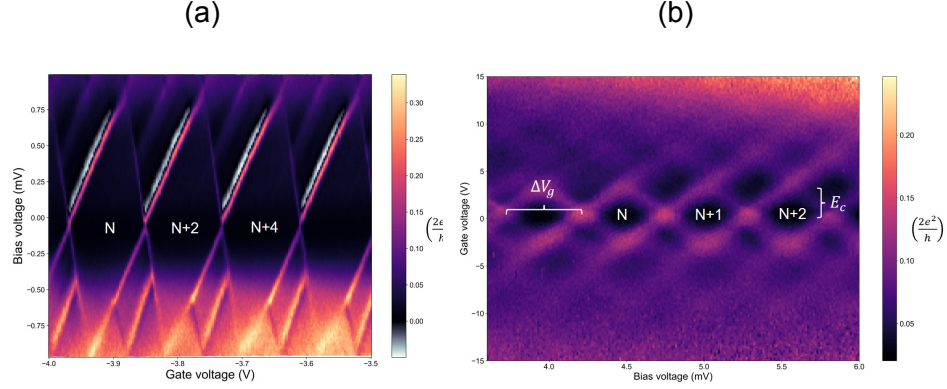
Figure 8: a) Coulomb diamonds in a superconducting island. Each crossing at zero bias are separated by two electrons. b) In a semiconducting quantum dot. Here each zero bias peak represent transport of a single electron.

initial charge, and V_j is the potential on j.

$$Q_i = \sum_{j=0}^{n} C_{ij} V_j + Q_i^{(0)} \tag{10}$$

The zero index represent the QD, while $i = 1, 2, 3, ..., n$ are the n electrodes coupled to the QD. By looking at the charge on the QD in eq.10 for $i = 0$ we can find the chemical potential on the QD in eq.11

$$V_0 = \frac{Q_0 - Q_0^{(0)}}{C_0 0} - \sum_{j=1}^{n} \frac{C_{0j}}{C_{00}} V_j \tag{11}$$

From here we can calculate the electrostatic energy needed to add N electrons to the quantum dot by integrating over the charge in eq.12.

$$E_{elstat}(N) = \int_{Q_0^{(0)}}^{Q_0^{(0)} - |e|N} V_0 dQ_0 = \frac{e^2 N^2}{2C_{00}} + |e|N \sum_{j=1}^{n} \frac{C_{0j}}{C_{00}} V_j \tag{12}$$

The total energy would be the sum of the kinetic energy and electrostatic interaction of all the electrons:

$$E(N) = \sum_{n=1}^{N} \epsilon_n^{(0)} + \frac{e^2 N^2}{2C_{00}} + |e|N \sum_{j=1}^{n} \frac{C_{0j}}{C_{00}} V_j \tag{13}$$

18

This is the energy of the QD with N electrons on it, but we are interested in the electrochemical potential of the QD, which in this model is given by eq.14.

$$\mu_N = E(N) - E(N-1)$$
$$= \epsilon_N + \frac{e^2}{C_{00}}(N - \frac{1}{2}) + |e|\sum_{j=1}^{n}\frac{C_{0j}}{C_{00}}V_j \tag{14}$$

There are two things to take from this equation. The charging energy of the island is the $e^2/C_{00} = eV_c$ term, and the lever arm of the different electrodes are given by $\alpha_j = -C_{0j}/C_\Sigma$. We have that $C_\Sigma = C_{00}$ is the sum of all the contributions to the capacitance. The lever arm tells us a story of how well capacitively coupled a specific electrode is to the QD. The electrodes are the gates, and the tunneling coupled source and drain.

The situations where we get zero bias conductance are when the chemical potential on the island is equal to the chemical potential in both the source and the drain. If we say that index $i = 1$ corresponds to a side gate, it is possible for us to expand the sum in eq.14 and find the gate potential needed to add one extra electron to the island at zero bias by setting $\mu_{N+1} = \mu_{S/D}$.

$$\mu_{N+1} = \epsilon_{N+1} + \frac{e^2}{C_\Sigma}(N + \frac{1}{2}) + |e|\sum_{j=1}^{n}\frac{C_{0j}}{C_\Sigma}V_j = \mu_s$$
$$V_g(N+1) = \frac{1}{|e|\alpha_g}\left(\epsilon_{N+1} + eV_cN - |e|\sum_{i=2}^{n}\alpha_iV_i - \mu_s\right) \tag{15}$$
$$\Delta V_g = V_g(N+1) - V_g(N) = \frac{1}{|e|\alpha_g}(\epsilon_{N+1} - \epsilon_N + eV_c)$$

In eq.15 we opened the sum to be able to pull out $V_{01} = V_g$ and the lever arm of the gate, $\alpha_1 = \alpha_g$. The last line is the spacing between two resonance peaks at zero bias. We can clearly see that it is similar to eq.7, but weighted by the lever arm of the gate. The same argument goes. If the quantum confinement is low compared to the charging energy, all the resonance peaks will be equally separated.

Furthermore, we can get equations for the boundaries of the diamond. Each of the four edges of the diamond corresponds to the chemical potential of the island to
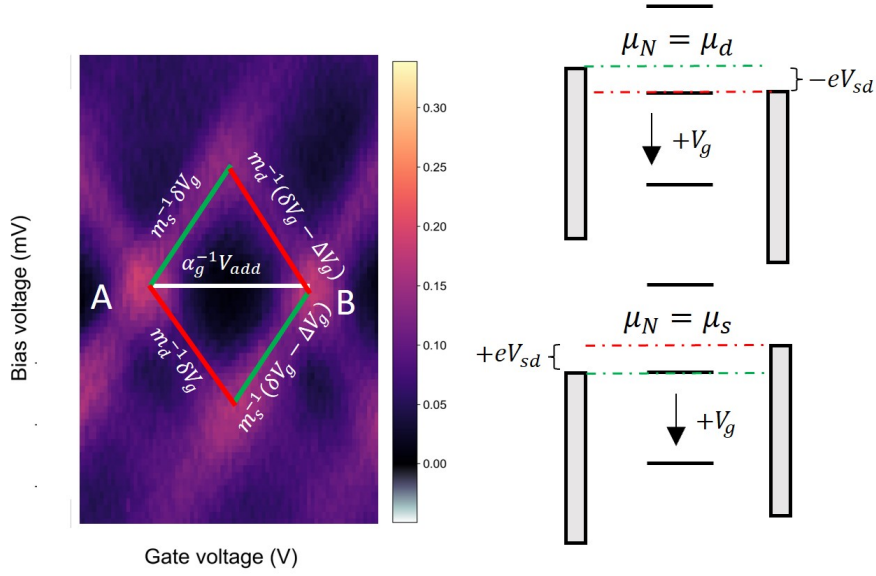
Figure 9: Equations for boundaries in the coulomb diamond. The two green lines represents the coupling of the source to the QD, only shifted by a value proportional to the resonance level spacing ΔV_g. Red lines are the same but for the drain. 'A' represents the origin of the diamond where $\delta V_g = 0$. 'B' is the origin of the next diamond ($\delta V_g - \Delta V_g = 0$). The two energy diagrams are the cases where we either follow the green line ($\mu_N = \mu_s$), or the red line ($\mu_N = \mu_d$). The sign on the bias and gate voltage is to emphasize where we are moving in the 2D diamond.

match that of either the source or the drain. Applying a positive gate voltage will move the states on the QD down in energy, and from the diamond we see that to stay on the edge we must match by either applying a negative or positive bias. The interpretation of this is that for a negative bias, the chemical potential of the drain and the QD stay aligned, while for positive bias the source stays aligned with QD, as depicted in fig.9.

In this setup, the source and drain are not always per the name the "source" and "drain". We could instead say contact one and contact two, because the electrons will flow in the direction based on the sign of the bias window. What is important to keep in mind is that the slope of the lines tell a story about the tunnel barrier, and how well the two barriers are capacitively coupled to the QD. If, for instance, the tunneling region has different thickness, we can expect there to be a tilt of the diamond. This we can calculate by finding δV_g, which is defined as $V_g - V_g^{(0)}$, where

20

$V_g^{(0)}$ is the potential where we have zero bias resonance peaks, ie. $\mu_N = \mu_s = \mu_d = 0$ (Marked 'A' in fig.9). We will then go on and define four boundaries. We have $\mu_N = \mu_s$, $\mu_{N+1} = \mu_s$, which are the green lines in fig.9, and $\mu_N = \mu_d$, and $\mu_{N+1} = \mu_d$, which are the red lines.

What we assume is that when we apply a bias, the source and the drain contribute between 0 and 1 each, but such that it adds up to the total bias. This we can write as $\mu_s = |e|V_s = |e|(1 - f)V_{sd}$, and $\mu_d = |e|V_d = |e|(-f)V_{sd}$, where f tells us how much the source or the drain contributes when applying a bias. In the anti-symmetric case they contribute equal in each direction, $\mu_{s/d} = \pm e/2 \, V_{sd}$.

$$\delta V_g(\mu_N = \mu_s) = \frac{1}{|e|\alpha_g}\left[\left(\epsilon_N + eV_c\left(N - \frac{1}{2}\right) - |e|\alpha_s V_s - |e|\alpha_d V_d - \mu_s\right) - \left(\epsilon_N + eV_c\left(N - \frac{1}{2}\right)\right)\right]$$
$$= -\frac{1}{\alpha_g}(\alpha_s(1 - f) - \alpha_d f + (1 - f))V_{sd}$$

$$\tag{16}$$

$$\delta V_g(\mu_N = \mu_d) = -\frac{1}{\alpha_g}(\alpha_s(1 - f) - \alpha_d f - f)V_{sd} \tag{17}$$

$$\delta V_g(\mu_{N+1} = \mu_s) = \frac{1}{e\alpha_g}\left(\Delta_{N+1} + eV_c\right) - \frac{1}{\alpha_g}\left(\alpha_s(1 - f) - \alpha_d f + (1 - f)\right)V_{sd} \tag{18}$$

$$\delta V_g(\mu_{N+1} = \mu_s) = \frac{1}{e\alpha_g}\left(\Delta_{N+1} + eV_c\right) - \frac{1}{\alpha_g}(\alpha_s(1 - f) - \alpha_d f - f)V_{sd} \tag{19}$$

Eq.[16-19] are the boundaries of the coulomb diamond. Δ_{N+1} is the level spacing $\epsilon_{N+1} - \epsilon_N$. Isolating for the source gives us the equation for the four lines in fig.9, where m_s and m_d are what is in front of V_{sd} in eq.16 and eq.17. For $f = \frac{1}{2}$ we can find the difference in the lever arm:

$$m_s(f = 1/2) = -\frac{1}{\alpha_g}(\frac{1}{2}\alpha_s - \frac{1}{2}\alpha_d + \frac{1}{2}) \tag{20}$$

$$m_d(f = 1/2) = -\frac{1}{\alpha_g}(\frac{1}{2}\alpha_s - \frac{1}{2}\alpha_d - \frac{1}{2}) \tag{21}$$

$$m_s + m_d = -\frac{1}{\alpha_g}(\alpha_s - \alpha_d) \tag{22}$$

$$\alpha_s - \alpha_d = -\alpha_g(m_s + m_d) \tag{23}$$

What eq.23 tells us is that from just calculating the slope of diamond can we find

the difference in the capacitance coupling between the source and the drain to the QD. In the case were they are perfectly anti-symmetric, ie. $m_s = -m_d$, this will be zero as expected. If we want to find the bias needed to add one electron all we need to do is see where eq.16 and eq.19 intersect (positive green and red line in fig.9).

$$eV_{sd} = E_{add} = \Delta_{N+1} + eV_c \tag{24}$$

Again we see in eq.24 that the addition energy consist of the quantum level spacing and the charging energy of the QD.

3 Fabrication of devices and measurement setup

3.1 Fabrication

All devices were fabricated on silicon chips where bonding pads had been made earlier by members of the same group. The blank silicon chips consisted of a 200 nm thick oxide surface, 48 bonding pads of gold and alignment marks.

Any design started off by transferring the wires of interest. The wires could, depending on what device would be made, be transferred at random, or selectively picked. In my case, the InAsPb double nanowires were first identified in the SEM, while all heterostructured ZB/WZ nanowires were picked at random. Every growth substrate generally followed the same pattern. A three by three pattern with precursor sizes ranging from one to nine (four by four ranging from 1 - 50 for ZB/WZ wires). In each section twenty by twenty of the same shot size could be found. The double nanowire lead island device had to be carefully search for before transferring because of low yield of islands. The ZB/WZ wires could be randomly picked as long as shot size were controlled.

The transfers were done using a micro manipulator, where wires were picked form the growth substrate (fig.10 a) and placed on the chip (fig.10b using a joystick to control a small needle (0.1 or 0.25 μm in diameter).

The next step were to image and position the transferred wires for the designing process. This was done using the E-line, which is an SEM with a laser controlled stage. The advantages of the E-line is that it can import the chip design file and align the design with its real space components. We can then go on to image the transferred wires, and the images will be positioned correctly in the design (with small errors that are fixed during designing). The design step is self explanatory. However, this step is the point where you want to take your time. Aligning the SEM images properly can save a lot of problems later.

Following the design is the exposing of it onto the chip. Prior to exposing, the chip has to be spin coated with a PMMA (polymethyl methacrylate) of approximately 300 nm thickness (fig.10c. This is the resist that the pattern is inscribed into. This is also a step where a lot of difficulty was met, primarily due to the small size of the chip (3 mm x 3 mm) which made the resist layer uneven at times. A two minute baking of the chip at 180^0C follows the spin coating to remove anisol solvent
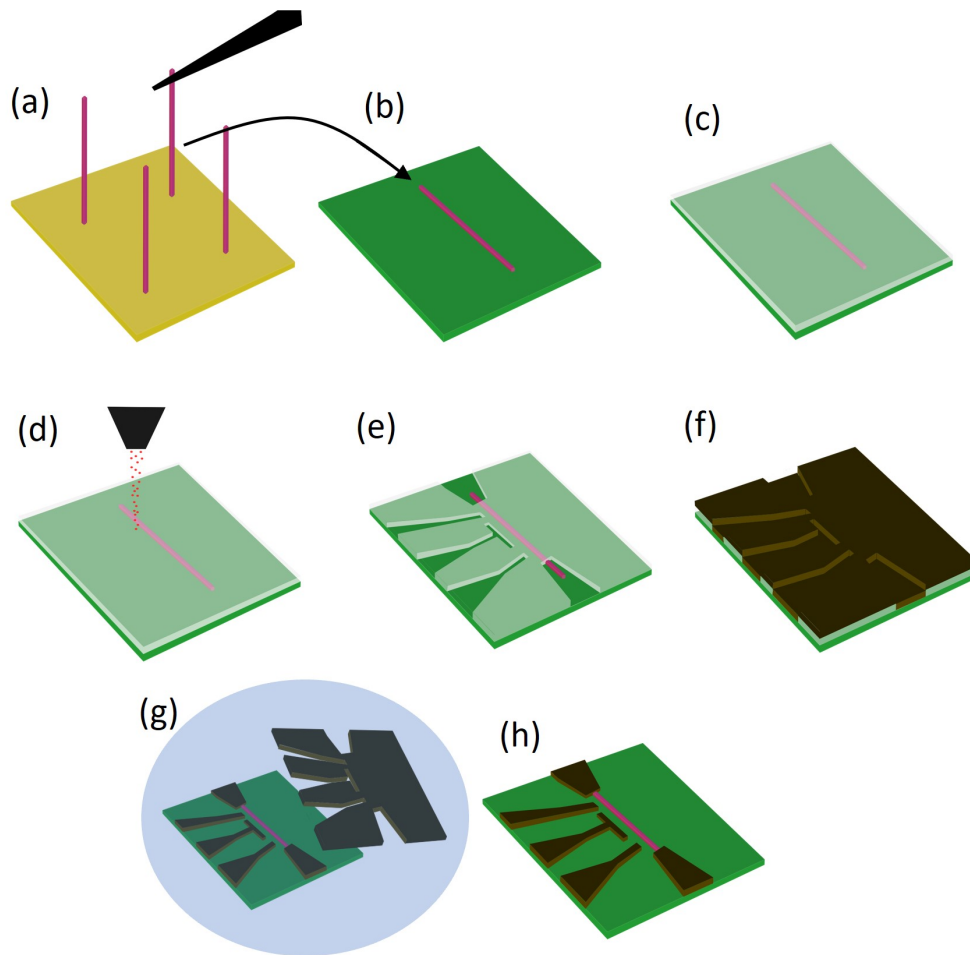
Figure 10: Fabrication steps from growth substrate (a) to finished device (h). a) Micro-manipulator picking up standing wires (purple) from the growth substrate (yellow) and transferring to the bonding chip (green) in b). c) A resist layer (transparent white) of PMMA A6 is spin coated on the whole chip. d) The EBL system exposes the pattern. e) Using MIBK:IPA 3:1 to develop the exposed pattern, f) Gold (dark yellow) deposited on the entire chip. g) During lift off the resist is removed and all the gold on top of the resist leaves the chip. h) Only the gold inside the pattern is left behind.

in the PMMA.

The exposing is done using the Elionix, which is an electron beam lithography system. It functions similarly to the E-line where a laser controlled stage ensures high precision patterns down to the size on only tens of nano meter (fig.10d. After

exposure, the chip is put in a MIBK:IPA (Methyl isobutyl ketone : Isopropyl alcohol) 3:1 solution where the exposed pattern is dissolved (fig.10e, and is followed by 30 seconds in IPA, some nitrogen drying and 45 or 60 seconds in a plasma asher. This step is called developing, which leaves behind the resist with trenches where the resist were exposed.

After the development of the pattern, 5 nm of platinum (functions as a sticking layer) and 150 - 200 nm gold is evaporated onto the chip using a physical vapor deposition (PVD) process (fig.10f. PVD is a process where a material is vaporized from a solid or liquid source and is deposited on a substrate[27]. Its a tool where a precise thickness of metal can be deposited. At NBI an AJA PVD system is being used for metal deposition. Prior to deposition an 8 minute Ar milling is done to remove the native oxide layer where the contacts will be deposited. The choice of gold thickness depends on the nanowire diameter. Generally you want the gold layer to be thicker than the wire. However, you also want there to be a lot of room between the top of the contact and the resist edge to avoid having gold in the trenches attached to the gold on top of the resist.

The last step is called liftoff, where the chip is placed in hot acetone to dissolve the remaining resist. While in acetone, a pipette can be used to create turbulence in the solution to 'blow' the gold off (fig.10g. I have done the liftoff with two different approaches. The first one I put the chip in 50^0C acetone for one hour before attempting to remove the gold. This worked sub optimal and I had a lot of liftoff issues in my first couple of devices. It is however fair to mention that choice of design could also have been the source of problems. A great rule of thumb is to not design multiple parallel lines over long distances.

The second approach to liftoff worked better. Two beakers with acetone were first heated to 60^0C. The chip was put in the first beaker after waiting for around 20 minutes (to ensure the acetone is warm enough), and I immediately started creating turbulence with the pipette. It is possible to check in the optical microscope if the liftoff has been successful by transferring the chip from the beaker to a watch glass with either acetone or IPA in it. It is important to constantly keep the chip either in acetone or IPA during the whole liftoff process. If it looks like all the gold on top of the resist layer is gone, a 30 seconds bath in IPA and 30 seconds drying in nitrogen and the liftoff is done. If there is still pieces of gold left, the chip can be placed back into the second beaker with acetone for as long as it takes (or until giving up), and

try again with the pipette. This second approach should be done under observation due to temperature exceeding the boiling point of acetone (56^oC).

The device is illustrated with a cartoon in (fig. 10h. At this point it is normal to go back to the E-line to check the alignment. The final step before loading the chip is to bond the 48 bonding pads to a daughterboard. The chip was glued to the daughterboard using a conducting silver glue. The bonding pads on the chip were contacted to the daughterboard with aluminium wires using an automated bonder.

3.2 Electron transport setup

The measurements were done in two different fridges for cooling, but the electrical setup is for the most part the same. The transport measurement setup is illustrated in fig.11. An alternating current (AC) on top of a direct current (DC) is pushed through a circuit that contains the NW. The setup starts with a digital to analog converter (DAC) or a Keithley as a DC source, and a lock in amplifier as the AC source, and they both meet up at a voltage divider. The voltage divider consists of an AC input and a DC input which contains a resistor that divides each signal with 10000 and 1000 respectively. The amplitude of a typical AC voltage after the voltage divider can range from 5 to 20 μV, while the DC voltage will usually stay within $\pm 20mV$. The output from the voltage divider is the source to the device.
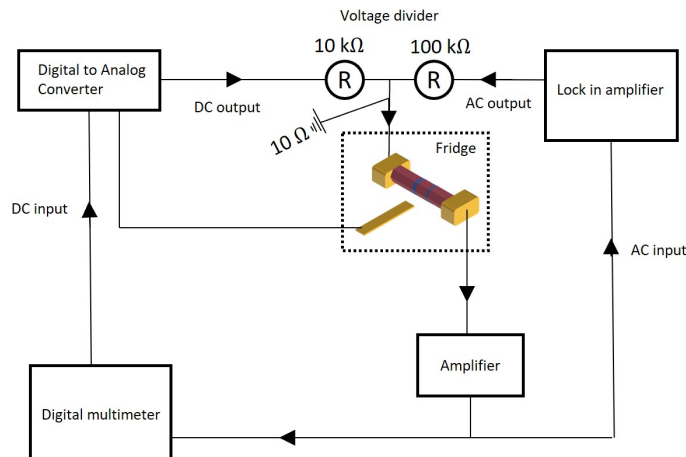

Figure 11: An illustration of the electrical wiring for measurements.

The fridge comes with a breakout box with 48 contact channels where the source

wire can be attached. Each contact comes with a lever that can either float or ground the contact. As the wire is hooked up to a contact and is put to float, a current flow through the device. Between the breakout box and the device, the current goes through a series of resistors and filters, followed by the aluminum bonds to the chip and gold contacts on the chip. After the current has passed through the device it moves out again in opposite order before exiting the fridge though the drain contact on the breakout box. It is the AC component which is measured to calculate the differential conductance according to eq.25.

$$G = \frac{\delta I}{\delta V} \tag{25}$$

After exiting the fridge, a current amplifier is next, which takes in the current and converts it to an amplified voltage output. The AC component goes back to the DAC for readout (and closes the AC loop), while the DC component is read out at a digital multimeter (DMM) which is connected to the DAC (or Keithley) to close the DC loop. In order to gate the devices, different channels on the DAC (or different Keithley's) are attached to the gate contacts though the breakout box. These contacts are not supposed to be a closed loop, but rather create an electric potential difference between the device and the gate. If the loop were to close through a leak, there is a chance of breaking the device.

The measurement's on the hetero-structure ZB/WZ nanowires were done in a Heliox AC-V cryofree system which allowed for cooling down to 2.6 K and 300 mK for limited periods.

The Pb island device were measured on in the Triton cryofree dilution refrigerator, where a mixture of ^{3}He and ^{4}He give a base temperature down to 10 mK. The temperature during these measurement's were done at 40 mK. The fridge also came with magnetic coils for magnetic fields along the z direction and x direction which can go to 8.5 T and 3.0 T respectively.

4 Hetero-structure ZB/WZ nanowires

My work have been to characterize hetero structured InAs/InAsSb nanowires with the goal of finding the ideal growth parameters. The different parameters explored have been precursor size, V/III flux ratio, barrier and dot length, pause length in intersection and temperature. TEM studies were done to determine size and symmetry of the two barriers, as well as how much the same dot varies from wire to wire. Electron transport were done at either 0.3 or 2.6 K to determine if we did in fact have a well defined QD. What we were looking for were an in-situ grown QD which is consistently working, but also easy to use (ie. we dont want a QD that needs ridiculously high negative gating to function).

Every growth were done with different precursor sizes, ranging from 1 to 50, which is an easy way to control the diameter of the nanowires. The number refers to the number of EBL shots used to expose a single precursor spot. For the rest of this thesis we will define the precursor size as a 'shot' number. The first set of devices were fabricated with a simple setup with source and drain, together with a backgate and sidegate. The TEM images taken prior to measuring identified two WZ segments separated by ZB part in all the wires, but none of the devices showed any resemblance of quantum resonances during transport measurements. The second set of devices had some fabrication problems which resulted in few working devices, but those that did work had the same result (nothing). At this point we speculated that the NW diameter were to large (around 200 nm in diameter), resulting in there being to many parallel charge carrier channels in the wire in order to pinch it off.

A problem with InAsSb ZB NW is that they seem harder to gate then pure InAs NW, which have been experienced earlier[28]. Thicker wires (around 200 nm in diameter) were for the most part impossible to pinch off. Charge carriers in InAs wires are located to the surface of the wire. The surface carriers are doping like such that there is high n - type conductivity, even in the intrinsic case. This is also enhanced when exposed to air[29]. A drawback of surface carriers is that the electron transport is more fragile to surface damage[30]. InAsSb ZB NW have shown to have lower resistivity and higher electron mobility than pure InAs [31][32].

Learning from these early sets of devices we decided to do a growth where the thinnest wires would undershoot preferable a lot, and the larges would be too big. We also decided with a constant V/III flux ratio and constant pause time in the

WZ/ZB transition. This time we would approach it a bit differently. We would first fabricate and do transport measurements in order to identify which quantum dots worked the best (if at all), and then characterize the dots in the TEM. All devices in this set of wires were fabricated by Xiangyu Lin, while transport measurement were done in collaboration.

These new sets of wires were grown with nine dots in three sections. The sections from bottom to top were done at 447ºC, 440ºC and 433ºC, and each section had three dots with different barrier growth time of 15, 10 and 5 seconds. We kept the dot growth time at a constant 30s, and the pause at 30s as well. The general design looks like the devices can be seen in fig.12a, which is a shot4 wire. The base ship where we design the devices only has 48 bonding pads, and therefor we designed a semi global side gate for each wire. Otherwise we see contacts for nine QD and four bare sections without a QD. These were meant to work as a reference.
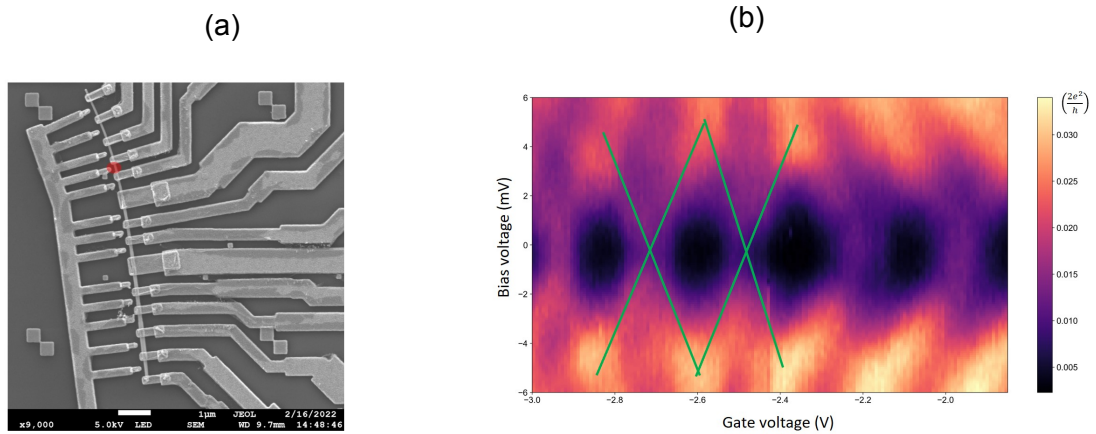
(a)   (b)

Figure 12: a) Overview of a device. Red dot is the corresponding QD to the diamond plot in (b). The scale bar i $1\mu m$. Image is taken by Xiangyu Lin. b) 2D bias vs gate voltage. Green lines to outline the diamond.

In fig.12b we have the diamond plot corresponding to QD8 which is marked in red in (a). What becomes apparent is that determining the charging energy will not be very accurate. This is the case for a majority of the diamonds, with some varying degree of how clear they are.

4.1 Transport

The first set of devices on this new growth were done on shot1. The data showed traces of resonances on almost all dots measured, but the data was generally noisy, and it was difficult to isolate the resonances from background. In the TEM it was pretty clear that the wires were not ideal. The wires could be up to 14 μm long, they were bent, and they had sections of radial overgrowth with the presence of bulges, especially at the later sections. The barriers were also quite long, which would increase the presence of stacking faults in the wire.

In fig.13a we see the resistance of the wires with different shot precursor. There is a clear grouping of good QD around the shot4 wires, with the highest amount of clear diamonds (7) colored in green. There are only wires with contacts that are plotted here, but for shot4 all the QD with contact experienced periodic coulomb resonances. Shot8 were a bit worse with only three good QD, while shot1 had a single one. The shot1 did show periodic resonances for a majority of the ones measured, but we only decided to do a 2D plot with resonance peaks we deemed 'good enough'. For the shot devices following shot1 we did 2D plots for all QD's that had periodic resonances. Both shot25 and shot50 were lacking any periodic resonances. This again we contribute to the thickness of the wires.

There is a sample size difference between the different shot numbers. Each set of devices contain 3 wires from the same shot number, and each wire had 9 dots. In total we had 27 QD for each shot. However, for shot1 we only got to measure on 10 dots, while only 5 of them had contact between the source and drain. The device 'blew' up while switching contacts for an unknown reason, and therefore cut the measurement short. The other devices did not blow up like shot1, so there are more plots per shot. However, there seemed to be a trend that the first wire we measured would have more dots with contact than the last. This has to do with us switching contacts at least 27 times in order to go through all the QD. We also had a global backgate together with a semi global sidegate, so any gate leakage could effect multiple dots.

From fig.13b, where the resistance is put in log, we can see a trend of lower resistance wires having less defined QD. The biggest problem with low resistance wires is that they require more gating to depleted for charge carriers. It is possible to have resonances on top of the background noise when there are multiple channels
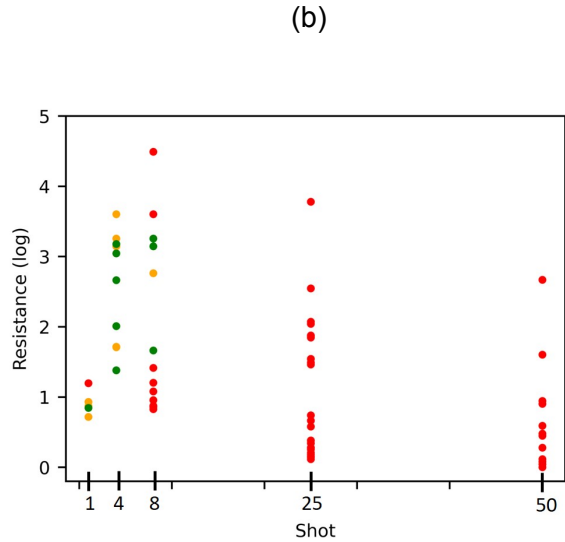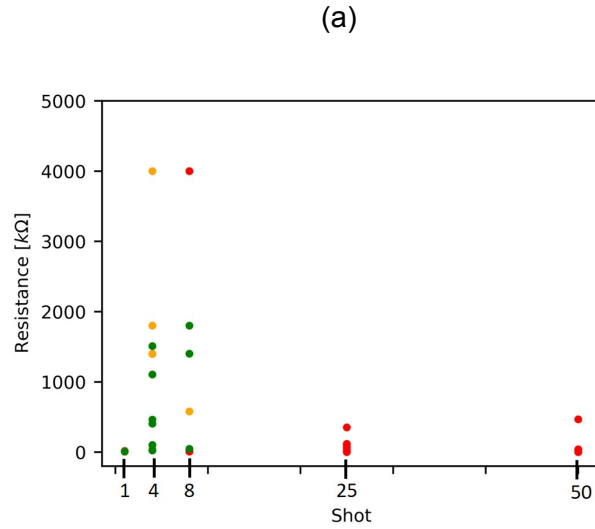
(a)

(b)

Figure 13: a) The resistance plotted for the different shot numbers. In green we observed resonances that were defined enough such that we could get a clear diamond plot. Orange are periodic resonances, but to noisy for any 2D plots. In red we observed no periodic resonances. b) Same plot but resistance is put in log.

for electron transport, but it is easier to disappear in the background when that is the case. Ideally we don't want to gate too much since we want the QD to be easy to work with in more advanced device designs in the future. We would expect the resistance to be quite large if we are in a coulomb blockade regime from the get go,

which we rarely are. The resistance also seem to drop with increased shot number, which is consistent with the larger cross section area and more charge carriers.

From the diamond plot we can extract a charging energy for each individual QD as seen along the y - axis in fig.14. On the x - axis we have the estimated charging energy of two plate capacitors as the source and drain tunnel barrier. The capacitance were estimated using $C_t = \epsilon_{InAs}\epsilon_o A/t$, where ϵ_{InAs} is put to 15.15. We assume that the gate capacitance is negligible. This we can check from the charging energy of the diamond. We can estimate the capacitance contribution from the lever arm of the gate. We know that $C_g = \alpha_g C_\Sigma$, and $\alpha_g = V_c/\Delta V_g$ (eq.15). With a charging energy around $3meV$, and a resonance spacing of $0.1V$ (smallest in this set of devices), we get a lever arm of 0.03. It follows that the gate capacitance is about 3 percent of the total capacitance.
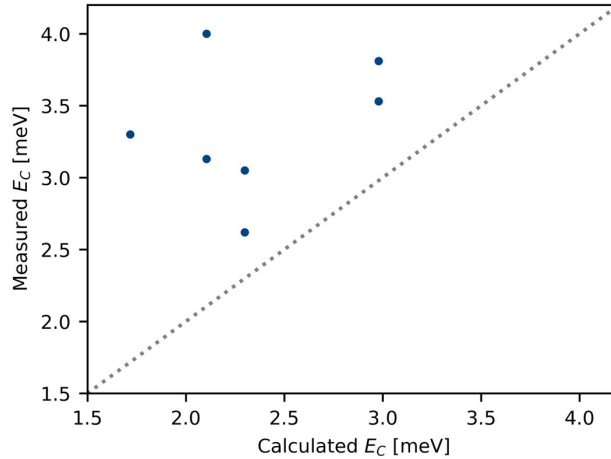

Figure 14: Measured charging energy plotted against estimated value for shot4 wires. Dotted line is the diagonal.

All of the shot4 charging energies extracted have reasonable values. The estimated charging energy depend on length measurement's done in the TEM, and those are not necessarily exact. If the real values are smaller then the measured we would expect the estimated charging energy to be greater. All length measurements were also done on same grown wire, and some variation is to be expected both in diameter and barrier thickness.

There are other ways of accidentally creating lateral confinement in the nanowire, like contact - contact confinement or two stacking faults in the InAs barrier. In order

to make a definite statement that the coulomb resonances observed are from the as grown QD's and not some other confinement, the QD length can be correlated with the gate capacitance. The longer the QD the and a greater gate capacitance is expected. In fig.15 are the shot4 gate capacitance against QD length plotted together with a linear best fit. The capacitance is normalised for a 100nm distance between the side gate and QD. The capacitance values are taken from the zero bias resonance peak spacing probed by the side gate, and the QD length's are taken from the TEM data. The normalisation were done due to the sidegate - QD distance ranging from 80 - 200 nm.
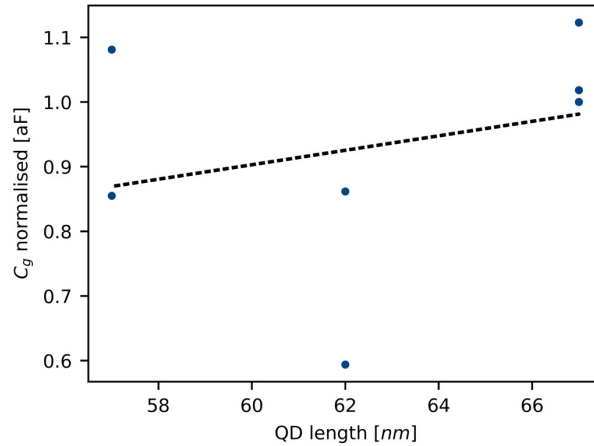

Figure 15: The normalised gate capacitance plotted against the dot length for the shot4 QD's. The dotted line is the best linear fit.

One of the problem with the data presented in fig.15 is that the QD length doesn't cover a big enough range. The QD were grown for equal time, but due to different growth condition and diameters along the wire there is some difference in length. Each sidegate are also not identical after lift off. In retrospect the data should have been gathered with the backgate.

4.1.1 Summary

We do have clear periodic diamonds, and generally it is over huge ranges like seen in fig.16, even though this one was especially clear and stable. The addition energy of all the diamonds stayed quite constant, which suggest the QD is not sufficiently

confined laterally. This could suggest that there the diamonds are not defined by a QD inside the barrier. The difference in charging energy between different QD depends on the diameter of the wire and barrier thickness. For future device design a deliberate QD length should be included to easier be able to verify that it is the as grown QD that we see. The QD should also be short enough such that we get a confinement along the growth direction and clear even/odd charging energy difference.
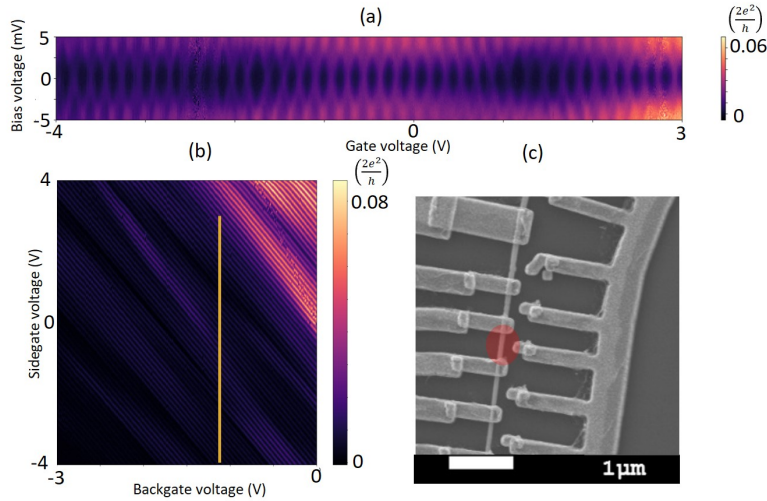

Figure 16: a) A diamond plot over a longer range for shot4 QD9 take along the yellow line in (b). b) A 2D plot of sweeps with the sidegate taken at different values of the backgate. c) SEM of the device with the QD marked in red. Taken by Xiangyu.

From transport measurements QD 8 and QD 9 from shot4 wires were the best. That would be QD grown at $433^{o}C$ with barrier growth time of 10 and 5 seconds.

4.2 TEM

In fig.17a wee see the length scales of barrier length and dot size for all the shot4 QD's. What to take from this plot is that section 1 seems to have more variation where we would expect there not to be. For instance, we would expect the QD length and QD width not to change much in the same section, because the only variable we change is the barrier growth time. Both section two and three looks a lot better in that regard. Another issue is that the first and second barrier generally have

different length in both section 1 and 2, but in section 3 they look to be overlapping nicely. This can be better illustrated in fig.17b where $\delta_{barrier}$ (eq.26) is plotted for each QD together with the square mean deviation.
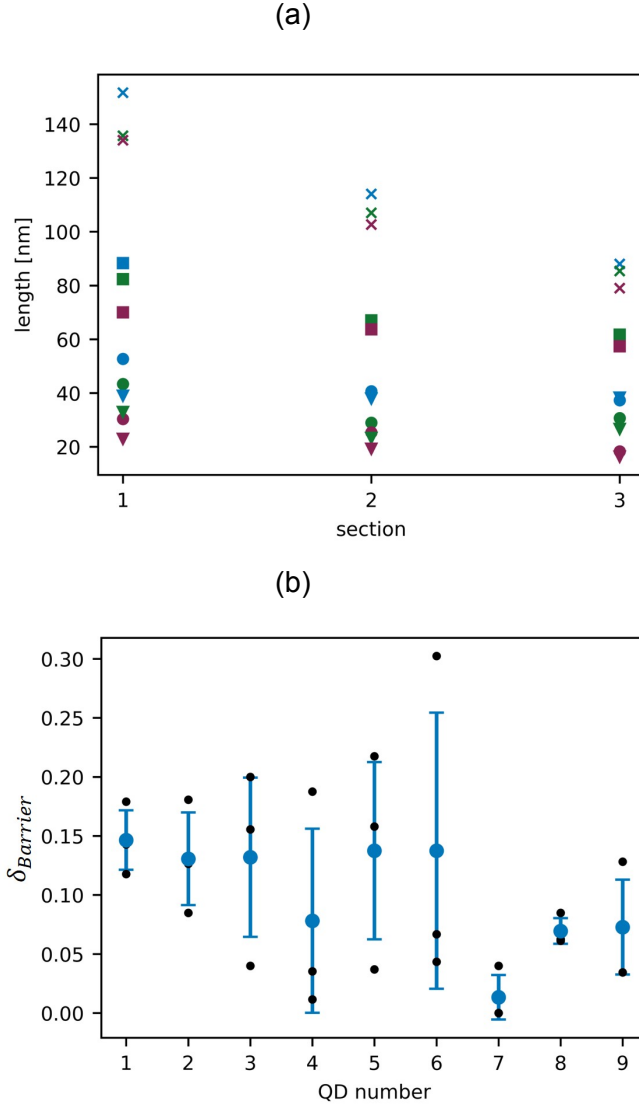
(a)

(b)

Figure 17: a) Length measurement's of shot 4 taken with the TEM for section 1(447°C), 2(440°C) and 3(433°C). The different barrier growth times are color coded with 15s (blue), 10s (green) and 5s (purple), while the markers represents wire width (cross), dot length (square), 1st barrier (circle) and 2nd barrier (triangle). All values are the average. b) The barrier ratio for the different QD numbers. Blue is the average value together with the square mean deviation.

35

$$\delta_{\text{Barrier}} = \frac{L_{B_1} - L_{B_2}}{L_{B_1} + L_{B_2}} \tag{26}$$

All three of the section 3 QD's (7, 8, 9) have a low $\delta_{Barrier}$ and the barriers seems to stay consistent between different wires. From this QD 7, followed by QD 8, seems to be the two best candidates. What fig.17b doesn't show is the actual length of the barriers, but for fig.17a the barrier growth times are well reflected in the actual length for all sections, and especially for section 3. We didn't have any diamond plots for QD7, and the reason for that could be the long barriers. This can be explained by there being a lot of stacking faults in wurtzite wires, and a longer barrier will in that case naturally have more. This can cause the formations of unwanted QD located inside the barrier.

The shot 4 devices were by far the best sets of devices in this work. There were a good number of devices with periodic resonances, but these were also cleaner, and it was possible to take plenty of 2D bias spectroscopy. The QD 8, which were grown at 433 degree Celsius, and with 10 seconds barrier growth, ended up with the best transport data. While going over the TEM images QD8 and QD9 on shot 4 also showed good symmetry between the two barriers, as well as little difference between different wires. Generally the dots grown at 433 ^{o}C looked good in the TEM, and since the transport data also favored them we decided to stick with 433 ^{o}C.

We also did measurement's on shot 8, but the data got worse. Shot 25 and shot 50 didn't show any resonances, and we suspect this has to do with diameter again. Not too surprising considering these wires are around 200 nm in diameter.

4.3 Conclusion

The transport data favored QD4, QD8 and QD9 on the shot4 wires. QD8 and QD9 also had good symmetry between the two barriers from TEM data. We can not say definitely that the QD are from the as grown wires, but this should be explored in future devices.

5 Double InAs nanowires with Pb island

In this chapter I will discuss the work done on a double InAs nanowire bridged by a Pb island. The double nanowire were grown in the MBE system where the Pb was epitaxially deposited without breaking the vacuum. The high T_c of Pb (7.2 K) and the corresponding high B_c [33] makes Pb a suitable superconducting material to take today's superconducting/semiconducting hybrid devices beyond the limitations of Al.

One theorized phenomenon to observe in a double nanowire hybrid device is the topological Kondo effect. The device first has to be in the topological regime with a magnetic field. The setup requires four Majorana zero modes (MZM), one at each semiconducting/superconducting interface. The device need at least three contacts with a tunnel coupling to the island, where two are the source and drain and the rest are grounded. When doing a temperature sweep of the differential conductance as the temperature is decreased one would see an increase in conductance at the Kondo temperature which saturates at a value depending on the inverse of the number of MZM. When the temperature is further decreased the system reaches a hybridization temperature where two MZM forms a non local topological degeneracy. This will remove the contribution from the two MZM to the conductance and there is a second increase of the conductance below this hybridization temperature. What makes such a observation exciting is that such a topological degeneracy is what is expected in a topological qubit system[34].

5.1 Superconductivity

The first microscopic theory of superconductivity was first published in 1957 by Bardeen, cooper and Schrieffer and is famously known as BCS theory. The theory was based on three understandings. There seems to be that the effective force between two electrons in a lattice can be attractive. This attraction comes from the phonons in the lattice. The second is that there is a stable state where two electrons at the Fermi surface pair up if there is an attractive force no matter how weak. The third and last is the construction of a coherent many particles wave function where the gap equation naturally pops out. An energy gap with energy 2Δ emerges in the energy band of a superconductor, which is the energy needed to break up a pair of

electrons, named cooper pair. Δ is the gap parameter (eq.27)[35].

$$\Delta = 2\omega_D e^{-\frac{1}{\lambda}} \tag{27}$$

Here ω_D is the Debye frequency, and λ is the electron – phonon coupling parameter. λ is very small in the weak coupling limit. *Pb* however is not a superconductor in the weak coupling limit and does deviate from BCS theory[36].

Cooper convinces us that there exists a bound state below the particle hole continuum for pair of electrons to form as a cooper pair. This quasiparticle state was described as a spin zero 'bosonic' lice particle, and therefore a pair of electrons can condensate into a macroscopic ground state. Due to off diagonal long range order, one cooper pair can be created in one area of the condensate, and a new cooper pair can be annihilated at the other end, and due to the coherent ground state this process will have a quantum amplitude and phase however far away from each other they are[35][37]. This process is what happens during an electron transport. The condensate can be assigned a complex order parameter, $\Delta = \Delta_0 e^{i\phi}$, with amplitude Δ_0 and a phase ϕ.

5.1.1 Andreev bound states

When an incoming electron from a normal metal approaches the superconducting phase (NS junction), but the energy is below the superconducting gap ($\epsilon < \Delta$), you would expect the electron to be reflected back at the interface. In reality there is a probability associated with the reflection either being the incoming electron, or a hole. If a hole is reflected back, a second electron is created inside the superconductor such that we have a cooper pair. The hole and electron are exactly time reversed quantum states, with opposite charge, momentum and spin[35].

Andreev bound states (ABS) can emerge at the NS interface due to spacial variation of the order parameter near the interface. The ABS is a sub gap state with energy below the superconducting gap that is a result of multiple Andreev scattering events, and are necessary for transport of electrons through a superconducting island inside the superconducting gap[38].

Due to available sub gap states in the Island it is possible for the superconductor to be in a state with odd number of electrons. This seems strange considering all the electrons pair up. The number of electrons on the island can be expressed

as (N_{cp}, N_e), where N_{cp} are the number of cooper pairs on the island, and N_e is the number of electrons, which is either 1 or 0 in this case. Depending on the energy of the sub gap state it is possible to either have $(N_{cp}, 0) \longrightarrow (N_{cp} + 1, 0)$ or $(N_{cp}, 0) \longrightarrow (N_{cp}, 1) \longrightarrow (N_{cp} + 1, 0)$ change in electrons on the island. In the first case the islands stays in an even state, while in the second case it alternates between an even and odd ground state. This can be better illustrated with an energy diagram of the even and odd ground states as seen in fig.18.
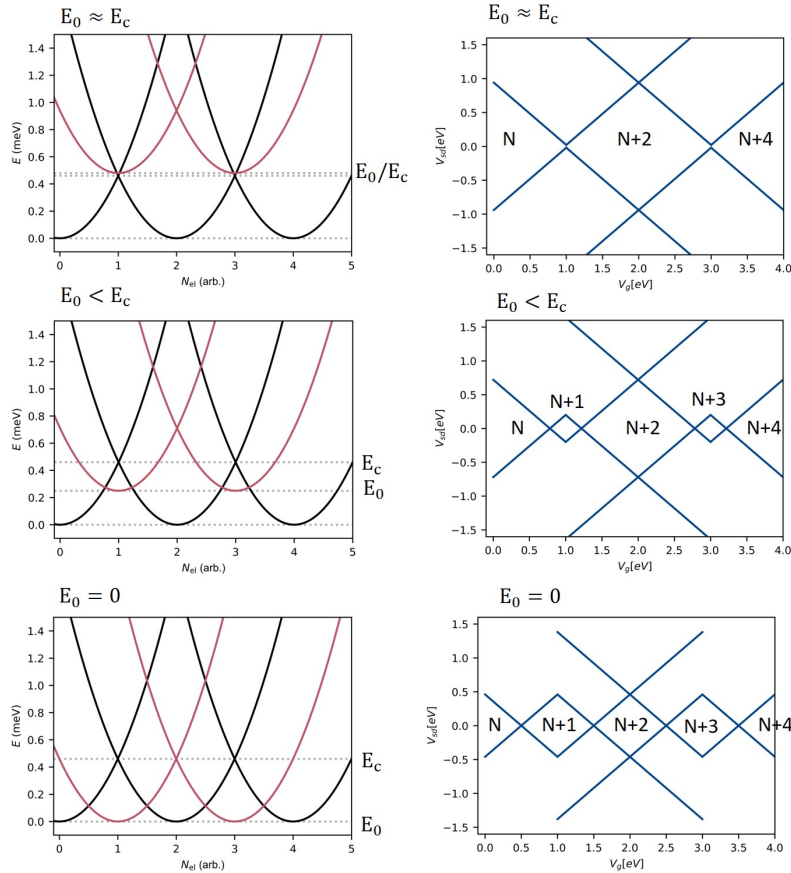

Figure 18: Energy diagrams of the even (black) and odd (red) ground state. The three situations are with $E_0 \approx E_C$, $0 < E_0 < E_c$ and $E_0 = 0$ together with the corresponding diamond pattern.

In fig.18 we can see the energy diagram for different energies for the ground state. In the first case when $E_0 \approx E_c$ the ground state will always stay in an configuration with even number of electrons on the island at zero bias. The corresponding diamond

plot would look like the panels on the right. Each diamonds figure comes out from subtracting the even energy parabola from the odd parabola. The diamond we see corresponds to the energy required to reach the sub gap state. In the $0 < E_o < E_c$ case we will have an alternating big/small diamond pattern with 1e population difference between the neighbouring diamonds. In the third case when $E_0 = 0$ we are in an even - odd region where the even and odd diamond have the same size.
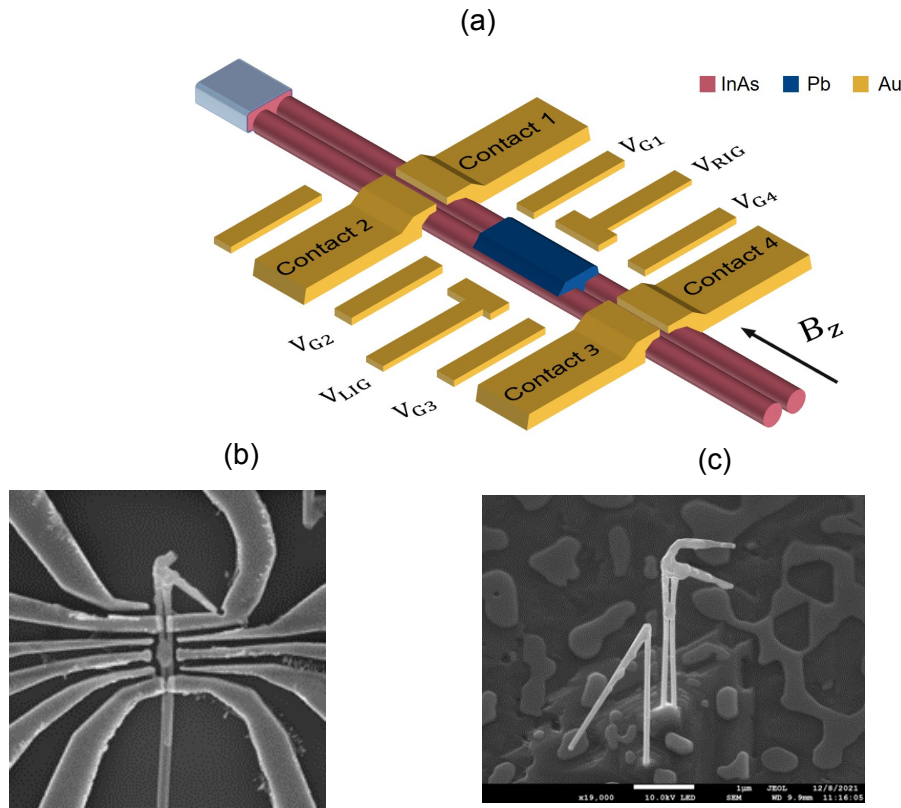
5.2   Device fabrication

Figure 19: a) An illustration of the device with labeled contacts and gates. b) SEM of finished device. c) SEM of the double wires standing on the growth substrate.

The double nanowire lead island device is shown in fig.19b. The goal of this growth sample were to create double NW with a single or double junction made from the shadow kink growth technique. A kink in the wire is induced by changing the growth condition such that the wire will start growing parallel to the surface. The kinked part will grow with equal probability in 6 direction corresponding to

the facets of the InAs WZ wire[39]. It is clear from the SEM in fig.19c that the front NW decided to kink in one of the three directions not fronting the double NW (lead is introduced on the front of the double NW with an angle off the surface). However, the lead is not a thin film covering the double nanowires evenly even though earlier growth has been done where that is the case [33]. What could be a reason for this is that the wires does not have obvious facets. A consequence of that could be that there are fewer low energy spots for the lead to attach too, and the most energetically favorable thing to do is for the lead to cluster. Where the lead collects doesn't seem to be entirely random either. A large amount of the wires were lacking lead along the legs, and whenever a shadow did induce a junction it became broader than expected. The reasons for there not being lead on the legs could be that the lead crawls to the substrate, and the same reasoning can be made for why the junctions grew thicker than expected.

In fig.19c the lead seems to have collected at the kink where there are more sharp corners and edges for the lead to collect, and the lead along the legs have crawled to the substrate. The result is that we accidentally got a lead island. The unfortunate result of the lead collecting though is that an otherwise thin film ($\approx 10nm$) is now considerably thicker. From other wires it also seems that the lead positions itself in the gap between the wires in the cases where that is possible, thus making the lead island possibly thicker than what we see. We did not measure the thickness of the lead section, and looking back now I do wish we did that.

The double nanowires were chosen because of the clearly separated wires, and what looked like a well defined island. The spacing between the two wires are crucial to avoid shorting them to each other. When the wires are removed from the growth chamber they immediately get in contact with oxygen in the air and form an oxide layer separating the two wires[40]. That is good for the wires, but not so good for the lead. Lead is very sensitive to water, and H_2O can actually be used for etching off lead [33]. This also puts a limitation on exposure to air, and much of the fabrication were done quickly after removing the growth substrate from the MBE chamber. Additionally, any storage were done in vacuum ($\approx 10^{-5}mBar$).

Another issue with Pb is that it start to dewett above 100^0C[33]. Dewetting is when the thinfilm start breaking up at form particles instead. Considering a step of normal fabrication is baking the PMMA resist at 180^oC, an alternative has to be done. We put the chip in vacuum for one hour after the spin coating to remove the

41

anisole solvent present in the PMMA before exposing in the EBL system.

5.2.1 Device configuration

The double NW device consisted of four contacts on each side of the island on both wires, named contact 1 - 4 in fig.19. Each contact came with a gate with corresponding gate numbering. Above contact two we also added an additional gate. We assumed that the double wire would be shorted across the kink part, and the 'kink' gate would attempt to pinch off any conductance over the top. We also added two island gate named Left Island Gate (V_{LIG}) and Right Island Gate (V_{RIG}). The device was oriented such that B_z ran parallel to the wires. There was also a global backgate.

Any measurement started with testing the limitations on the gates. We ruled out the backgate immediately from leaking. Luckily none of the contact pairs were shorted across the metal. V_{g1} were leaking at any voltage, and V_{g2} were limited to $\pm 2V$. The rest of the gates could be pushed to the max ($\pm 10V$). We quickly learned that V_{RIG} functioned like a global gate and could be used to pinch off what I would assume to be the right wire. The V_{LIG} were for the most part probing the island states. Any of the contact gates on the right wire were gating fine, but we couldn't pinch off completely to contact 1. From hooking up any combination of contacts we learned that there were a QD near contact 4 that we could probe on and off resonance. We see this from fig.20 where any combination that includes contact 4 show the same features, which suggest we are transporting through the same island. What we see are weak island resonances along the diagonal, and the vertical lines corresponding to a QD. Any combination not including contact 4 looks like the one in the bottom right corner. We do see the resonances from some conductance through the island, but the picture is dominated by the background. In the contact 1 - 2 setup, which is not shown, we cant see any resemblance of resonances which can suggest any conductance is over the top.

From fig.20 we can assume contact 4 is weakly coupled to the island while the remaining three contacts are strongly coupled. We can not tell if we actually managed to create a low coupled tunnel region from contact 1 to the island due to the short over the top. Actually, since the 'kink' gate couldn't pinch off and V_{G1} was leaking there were no way to weakly couple from the top. The same was true with contact
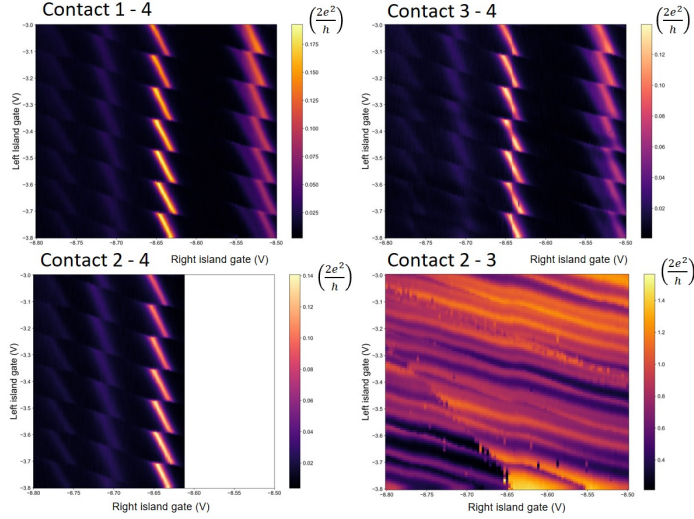
Figure 20: Four contact combinations with a 2D map of V_{LIG} in steps of V_{RIG}. Contact 2 - 4 is partially finished due to aborting the measurement early.

3 since V_{G3} was limited to $\pm 2V$. This will be visible in any diamond measurement where the lever arm of the source and drain will be clearly different due to the tilt (eq.23).

5.3 Magnetic field dependents

We did magnetic field dependent measurements in gate configuration yielding different coupling to the island. We tuned the coupling with V_{RIG}. In fig.21 a 2D map with the two island gates show how a QD could be tuned on and off resonance with V_{RIG}, while V_{LIG} could be used to sweep the island while effecting the QD to a lesser degree. The further left we were in this picture the less coupled we were to the island (at least from one side). The periodic resonances laying almost horizontal seem to go away towards greater negative V_{RIG}, but in reality the diamonds are pulled apart such that there are no longer zero bias resonances. The data presented here were all taken between contact 3 and 4.

5.3.1 Less coupled region

The 2D plot of V_{LIG} in steps of parallel magnetic field can be seen in fig.22. What we see are 2e spacing at 0 field that evolves into 1e spacing after 0.25 T. There are
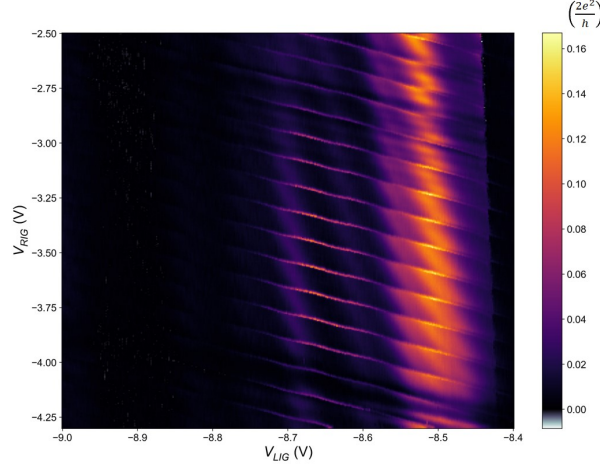
Figure 21: A gate map when sweeping V_{LIG} in steps of V_{RIG}.

three region of interest in this plot marked by a line below the plot. The first region contains coulomb resonances with 2e spacing. Reaching the end of this region we see a secondary more faint line appearing between every primary line. These lines stem from what is called quasiparticle poisoning[41]. They suggest in this paper that the poisoning can come from high energy electrons (or holes) in the leads to the island, tunneling into the BCS continuum of the superconducting island. These high energy particles will relax down to the edge of the superconducting gap at Δ. A shadow diamond will appear in the bias spec as an identical diamond, but shifted 1e.

Following this we have the even odd region marked by 'II' in fig.22. What happens here is that the island can be in either an even state with only paired up cooper pairs, or an odd state where there is also a single electron on the island. Due to cooper pairs having opposite spins, the even state will not be affected by the field. The odd state on the other hand will be moved down in energy with the magnetic field. This is illustrated in fig.23, where we see the even and odd parabolas for the primary state and the poisoned state.

As we increase the magnetic field, the red and yellow lines are moved down. The system likes to be in the lowest energy state while moving along the x axis (gating). If the primary odd parabola (red) is above where the two even parabolas meet the system will only stay in the even ground state, and every electron transport comes
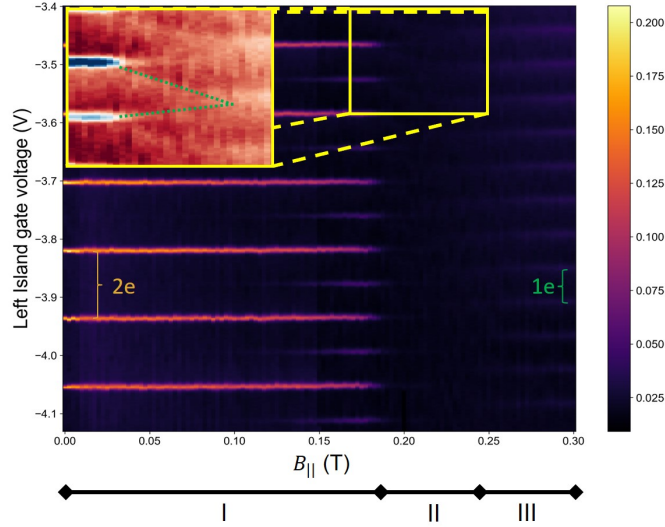
44

Figure 22: Sweeping the left island gate under different magnetic fields parallel to the double wire. The inset is the marked region but saturated and rooted to better see the resonance peaks in the even-odd region. Dotted green lines are there to guide the eye. Below the figure we see a representation of the three regions. I: even - even, II: even - odd, III: normal.

in pairs. This is what happens in the first region. The transition from the first to the second region is the point when the bottom of the red parabola is resting exactly where the two even parabolas cross each other. As soon as this happens the resonance peaks will split as you see in the inset in fig.22, and about a third into the second region we have the situation illustrated in fig.23 and the corresponding resonance peaks below.

One note about the poisoned state. In [41] they explain that the amplitude of the poisoned state corresponds to a poisoning time of the excited state, τ_p. This parameter tells us how long time it takes to change the occupation of the excitation, and is tuned by how well coupled the leads are to the island. Strong coupling will give a low τ_p and more poisoning, and opposite is true for low coupling. It is enough that one of the leads are strongly coupled to get substantial poisoning, and judging by the tilt of the diamonds it is fair so say that either the source or drain is more capacitively coupled to the island with a smaller lever arm. The poisoning rate of an island is expected to increase with a magnetic field (τ_p decreases) [42], which is why it only seem to appear at $B_{||} \approx 0.11T$. However, there is probably poisoning
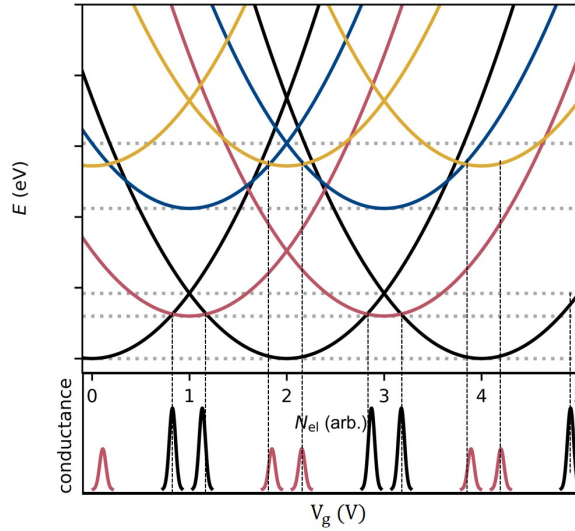
Figure 23: Charge-state energy diagrams as a function of energy and the number of electrons on the island. The number is arbitrary, and 0 is in reality N electrons. Each parabola represent a state. We have the even primary state (black), the odd primary state (red), the even poisoned state (blue) and the odd poisoned state (yellow). When two line cross electron transfer takes place. Below the energy diagram we see the corresponding 0 bias peak that would appear when sweeping the gate voltage.

below all the way down to 0 field, but hidden in the noise.

In the third and final region of fig.22 we have equally separated resonance peaks for 1e electron transport. This could be the island turning normal, but a B_c of only 0.25 T is way below previously reported values of more than 8.5 T [33]. However, the thinfilm of lead presented in [33] was around 9 nm thick, while the island in this device is considerably thicker than that. They also reported a B_c of about 0.8 T for a thinfilm with 50nm thickness. Another indication that the superconductivity is gone above 0.25 T is that the even - odd spacing stays equal[43] and no obvious oscillations can be observed which would suggest the device is in the topological regime as would make it more interesting[44].

Another observation is that the conductance is heavily suppressed inside region 'II'. One way to think of it is that as the island goes from region 'I' to region 'II' the system changes from transport being cooper pair driven to single electron channels, and as we enter region 'III' the metal turns normal. One possible explanation is that

46

inside region 'II' electron transport happens through ABS's located at each end of the island. From the earlier discussion on device fabrication I argue that we have a well defined QD near contact 4 that we are probing in and out of coulomb blockade with V_{RIG}, and we effectively have a low coupled contact. The remaining contacts are strongly coupled. In such a situation two ABS's, one at the QD and one at the 'open' side can have different energy, and this energy difference will suppress the conductance across the island while in region 'II'. Once we reach region 'III' the sub gap state reaches zero energy and conductance is turned on again [45]. The requirement however is that there are two localized ABS's at each end, but for shorter islands lengths the wavefunction of the two ABS's could overlap and instead we have a delocalized ABS accessible from each end of the wire and its simply a situation where cooper pair electron transport through the island is a fast process while the single electron transport is slow.

The 2D plot in fig.22 corresponds to a region where the island is in a region where $\Delta, E_0 > E_c$. This can be seen from the 2e spacing of the resonances, but also from the fact that the charging energy is $0.46meV$. The charging energy can be found from the height of the diamond. In the 2e region the height correspond to adding two electrons, and therefor is $2E_c$. Unfortunately we didn't have any NS devices in this set of devices such that we could extract Δ, but earlier reported values lay above $1meV$ [33]. We do see a splitting of the 2e to 1e resonances above the $\approx 1.1mV$ in fig.24, which can be explained with transport above Δ. The energy of the sub-gap state can be put in the range of the charging energy due to the two tips of the diamond touching.

5.3.2 Low coupled region

When decoupling the island by applying a more negative voltage on all the gates we observe a splitting of the diamonds. In this regime the energy of the sub-gap state is also greater than the charging energy of the island ($E_0 > E_c$). The splitting of the diamonds is suggested to come from the coupling of a QD to the island from one of the leads. In [46] he talks about a S-QD-S system where such a splitting of the diamond is observed in the low coupled regime. However, he only talks about quasiparticle transport which puts a lower bound on the diamond tip at 2Δ. This is because the bottom of the gap of the source superconducting lead has to be in

resonance with the QD level, which also has to be on resonance with the top of the superconducting gap of the second superconducting lead. Even though we have not measured Δ, we are in the regime where $\Delta > E_c = 0.46 meV$, so that explanation alone doesn't work.
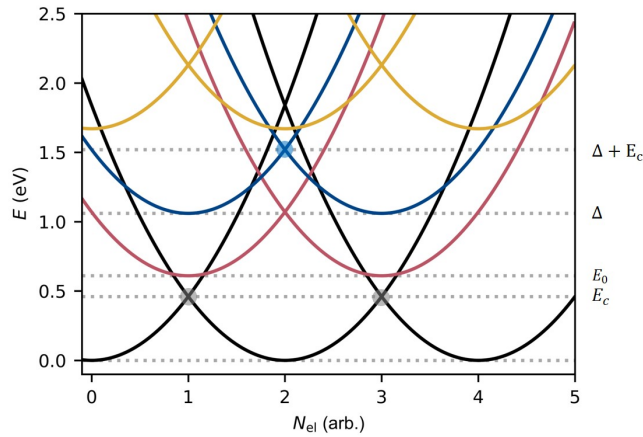
[47]

(a)
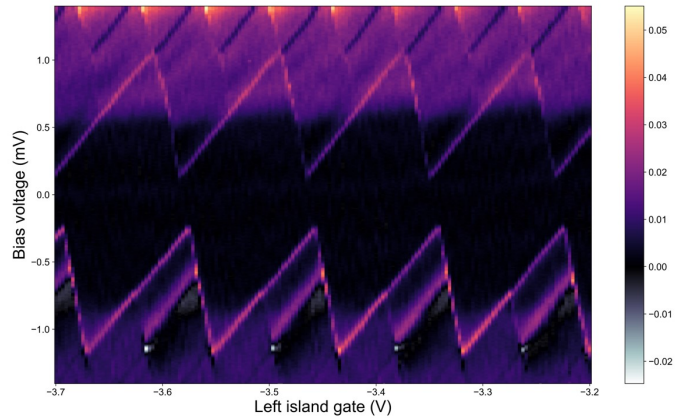
(b)

Figure 24: a) Coulomb diamonds in a more decoupled gate configuration. The inner diamond peak separation, marked in red, and the outer diamond peak separation marked in green. b) The parabola setup for the diamonds in (a)

In [47] they saw the same phenomenon with a splitting of the diamond in a

48

carbon nanotube coupled to a superconductor and a normal lead. Again the tip of the diamond is suppose to rest on 2Δ, but they also saw weaker suppressed resonances inside the gap, and at 0 bias they contributed the conductance to come from the QD level being on resonance with the subgap state allowing 2e transport. The diamond tips they observed for $0 < V_{sd} < 2\Delta$ they explained came from phonon mediated resonant Andreev tunneling. The requirement is that $\mu_S < \mu_{QD} < \mu_N$, where $\mu_{S/QD/N}$ is the chemical potential of the superconducting subgap state, QD and normal lead. The reason we don't see any 0 bias resonance as they did might do with our configuration. The V_{LIG} probes the energy of the ABS, but is so far away from the QD that it doesn't affect μ_{QD}. This we already know from fig.21. As we move away from the vertical resonance levels by going more negative on V_{RIG} a bias is required to reach the μ_{QD}. A different reason might be that the conductance is already very low in this low coupled regime, and the even more suppressed resonance Andreev tunneling is hiding in the noise.

The gap in the diamond makes it hard to do a gate against magnetic field similar to fig.22. We do see the resonances after the lead turns normal around 0.25 T. (see supplementary) Instead, by making diamond plots in steps of magnetic field it was possible to extract how the energy of the sub gap moved with the magnetic field by looking at the gap spacing which is plotted in fig.25. Both the inner and outer peak spacing follow the same trend which could indicate that we are probing μ_{QD} with the magnetic field.

5.3.3 effective g-factor

From the inset in fig.22 we can see two line splitting with the magnetic field almost linearly. From these two lines can we calculate an effective g-factor of the E_0 state in the even - odd region.

$$\Delta E = g^* \mu_B \Delta B_{||} \tag{28}$$

In eq.28 we relate the energy gap with the magnetic field, the bohr magneton (μ_B), and the effective g - factor (g^*). Since we are extracting from fig.22 where we are sweeping the island gate in field, we need to multiply the energy with the lever arm such that we get $\Delta E = \alpha_g \Delta E_g$. The even odd splitting evolving in $B_{||}$ is plotted in fig.26a) for less coupled region and g^* can be calculated along the red line. From
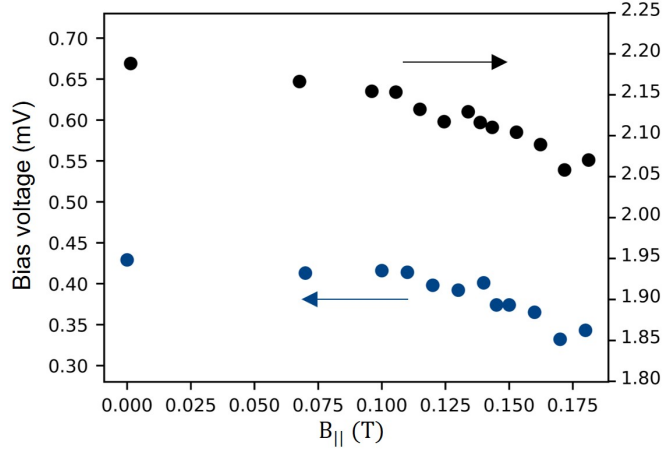
Figure 25: The spacing between the inner (blue) and outer (black) diamond peaks. Arrows point to corresponding y value.

this we get a g^* of 114. This is not necessarily too big considering Pb has large spin orbit coupling. In the more coupled regime (fig.26b) the even-odd splitting region lasts over a wider range in B-field, and we get a corresponding lower g^* of 15. This could indicate that the state in (b) is less proximiticed by the Pb than in (a). In [48] they see the opposite, that more negative gate lowers g^*. However, they used Al as a superconductor with $g^* = 2$, while Pb has strong spin orbit coupling and would expect a greater g^*.

In fig.25 we see how the diamond tips evolves with magnetic field in the 2e even region, and assuming it is linear we can extract a $g^* \approx 4$. That is a reasonable value for a hybrid system with the bulk g^* of InAs to be -15[49]. An other explanation could be that we are moving μ_{QD} with the field. Even though we cant see anything in the even odd splitting region due to conductance suppression, we do know that the resonances go from 2e spacing to 1e spacing similar to fig.22. There seems to be a change of g^* with the magnetic field. A possible explanation is that when $E_0 = E_c$ single electron transport becomes permitted inside the gap, and if the conductance was not suppressed in the even-odd splitting region we would see that the diamond tip's touch.
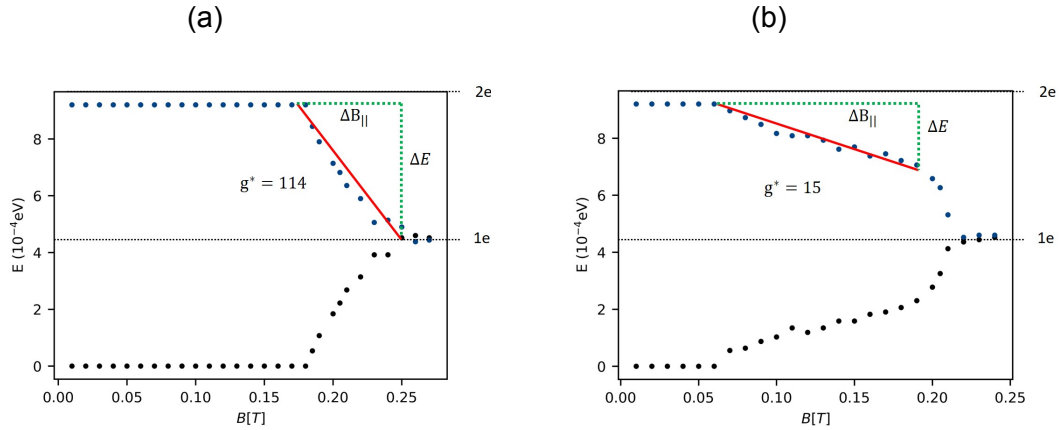
Figure 26: a) The even and odd spacing from fig.22 as they split with magnetic field. Red line indicate a state moving in field with a g^*. b) Similar but for a region where we are more coupled. The energy has been corrected for the lever arm of the gate's.

5.3.4 Final thought

There is the possibility that the even - odd region start splitting because Δ becomes smaller than E_c and we are really seeing the gap closing. The red parabola in fig.23 could correspond to bringing down the gap instead of a subgap state.

5.4 Temperature dependence

Since poisoning earlier have been proposed to stem from high energy electrons in the leads of the island, we wanted to see if increasing the energy of the system with temperature would excite more poisoning. In fig.27 can we see how the resonance peaks starts to broaden around 300 mK. This suggest that the broadening is coupling dominated below, and temperature dominated above. The broadening continues up until around 1.3 K where the whole plot becomes a fog of background conductance. The same plot can be seen on the right, but with the color values tuned to enhance features. Below we have a line trace along the green line where we can count twice as many resonance peaks.

There is the possibility of the island turning normal and therefore breaking up the 2e spacing into 1e, but a T_c of 1.5K is a drastic reduction from the bulk value of 7.2 K [33]. A more satisfying explanation would be that we actually do see the
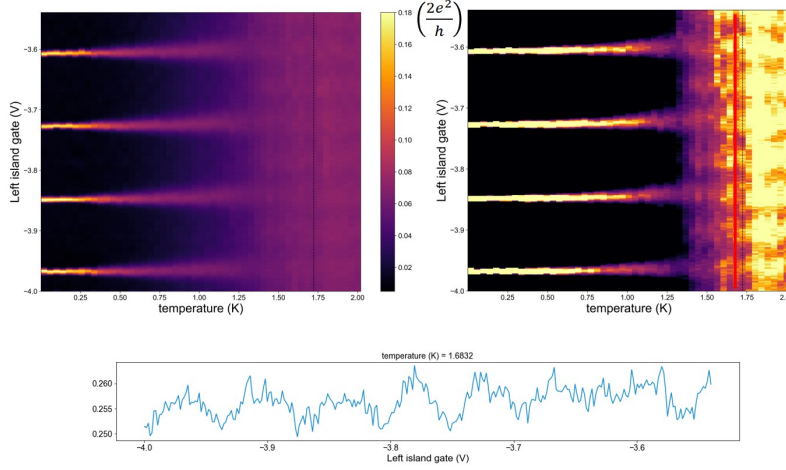
poisoning at elevated temperature.

Figure 27: Top left corner is a 2D plot of V_{LIG} in steps of temperature. Corresponding plot put in root and conductance max and min pixed around resonances to enhance features. Line trace where green line is in the right image.

A sweep of V_{LIG} in parallel field in three steps of temperature is plotted in fig.28, where the plots at different temperatures have been put over each other for easier presentation. The thermal broadening makes similar plots at higher temperature too smeared out, and it is already a problem at 1K above $B_{||} = 0.25T$.

We can observe in fig.28 that the primary resonance conductance is reduced earlier with increasing temperature, and for 1K it looks like the shadow state has equal amplitude to the primary resonance above 0.13 T. The poisoning time is expected to go down with increased temperature [50]. What we also see already at 0.6 K is that the conductance suppression inside the even - odd splitting region is less. If we assume that the suppression is due to two ABS's at each end of the island being off resonance with each other [45], a broadening of the levels could make them overlap more and reduce the exponential suppression.

5.5 Summary

In summary we have a device with one contact that can be pinched off, but due to faulty gates and shorting across the kink part of the wire a four contact device functions more like a two contact. We have localized a QD in the right wire which
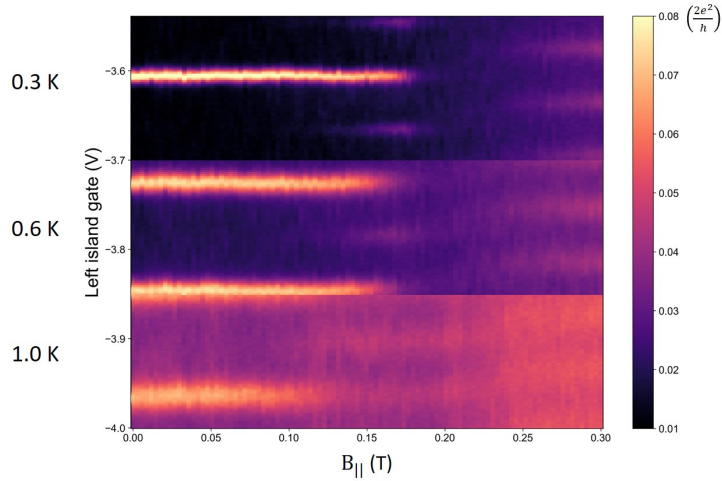
Figure 28: Sweeping V_{LIG} in steps of $B_\parallel$ at 0.3, 0.6 and 1.0 K. The plot at different temperature are overlapping, but the color scale and both axis are the same.

can be probed on and off resonance to control the coupling between the contact and the island. We can not extract a $\mathsf{B_c}$ or Δ from the data presented here, but it is suggested $\mathsf{B_c}$ is somewhere around 0.3 T due to the 1e spacing of the resonance peaks and no indication of entering the topological regime. A low $\mathsf{B_c}$ does make some sense in the context of the morphology of the Pb island. What we can say about Δ is that it is greater than the charging energy of the island because of the 2e resonance spacing at zero field.

6 Summary and outlook

In my work we have presented as – grown axial QD with the suggested growth parameters for the next set of devices. As this is written a new growth is already finished and the fabrication is under way. The natural next step would be to combine the as grown quantum dots into hybrid semiconducting/superconducting hybrid devices.

One potential device where as grown quantum dots would be of great advantage is the cooper pair splitter. Parafermions are suggested as a qubit in a topological quantum computer, and theory suggests that they could be realized in a cooper pair splitter. The device consists of two parallel nanowires bridged

by a superconducting material. There would be two normal leads, one at each wire, and one common superconducting lead. In the NS interface at each wire, we place our as grown quantum dots. The requirement of a high B-field makes Pb the a good candidate as superconductor for realizing such a device with its large B_c [12].

7   Appendix

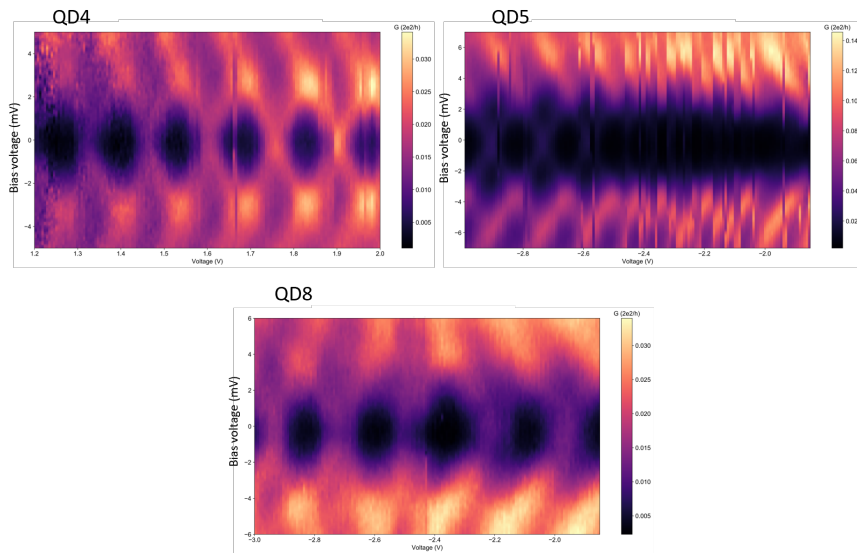## Appendix A: shot 4 coulomb diamonds

(a)
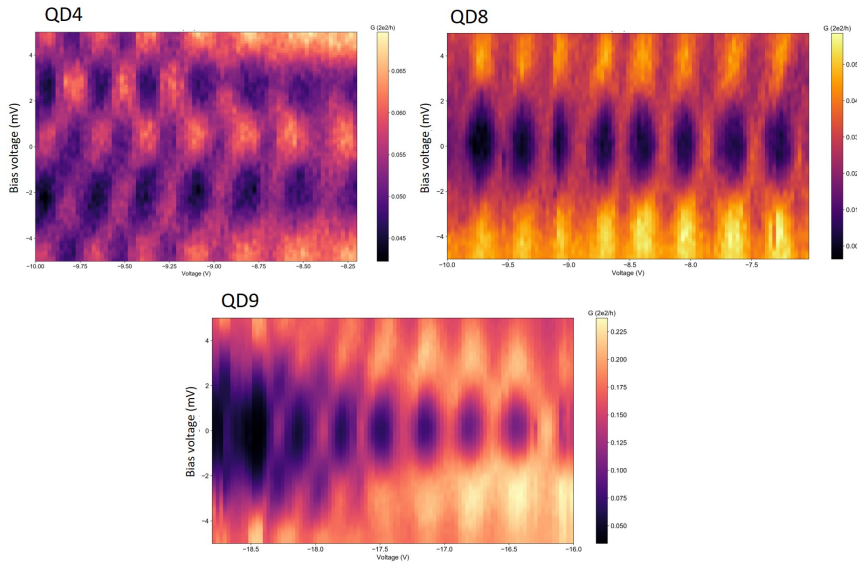
(b)

Figure 29: a) Diamond plots from shot4 2C wire. b) Diamonds plots from shot4 3A diamonds.

Appendix B: Shot 4 data

QD	E_c	Dot length [nm]	Gate - dot distance [nm]	Normalised C_g [aF]
2C dot4	2.62	67	175	1.02
2C dot8	3.53	62	175	0.86
2C dot9	3.25	57	175	0.85
3A dot4	3.05	67	100	1.12
3A dot5	3.3	67	100	1.00
3A dot8	3.81	62	90	0.59
4B dot9	4.02	57	140	1.21

Figure 30: The data presented in fig.14 and fig.15.

QD nr	Temp [celsius]	avg. 1st barrier [nm]	avg. 2nd barrier [nm]	avg. QD length [nm]	avg. QD width [nm]
1	447	53	39	88	152
2	447	43	33	82	136
3	447	30	23	70	134
4	440	41	38	67	114
5	440	29	23	67	107
6	440	25	19	64	103
7	433	37	38	61	88
8	433	31	27	62	85
9	433	18	16	57	79

Figure 31: The data presented in fig.17.

Appendix C: Calculating effective g - factor

More coupled region

$$g^* = \frac{\Delta E}{\mu_B \Delta B} = \frac{1.1 \times 10^{-4}}{\mu_B \times 0.13T} \approx 15 \tag{29}$$

Medium coupled region

$$g^* = \frac{\Delta E}{\mu_B \Delta B} = \frac{4.6 \times 10^{-4}}{\mu_B \times 0.07T} \approx 114 \tag{30}$$

Weak coupled region

$$g^* = \frac{\Delta E}{\mu_B \Delta B} = \frac{4.3 \times 10^{-5}}{\mu_B \times 0.18T} \approx 4 \tag{31}$$

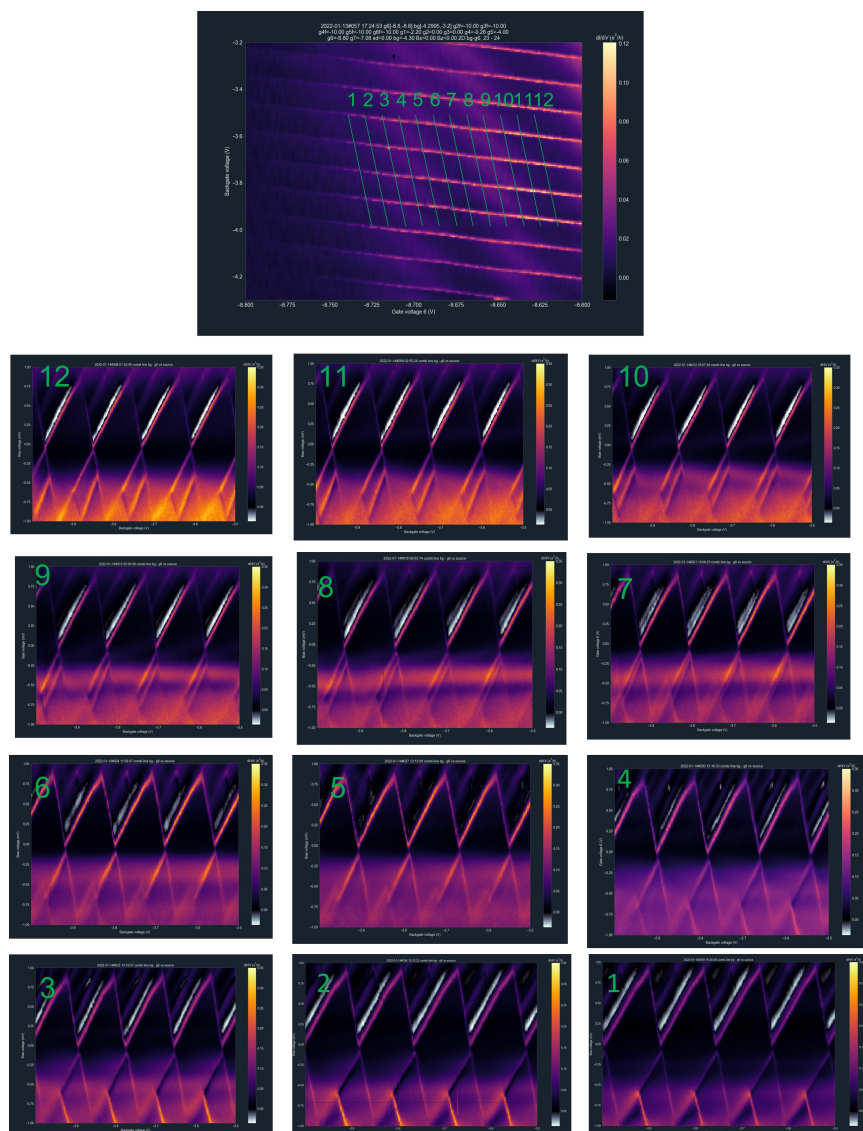# Appandix D: Coulomb diamonds across QD resonance

Figure 32: 2D of bias voltage against V_{LIG} at different V_{RIG} values as marked on the map above.

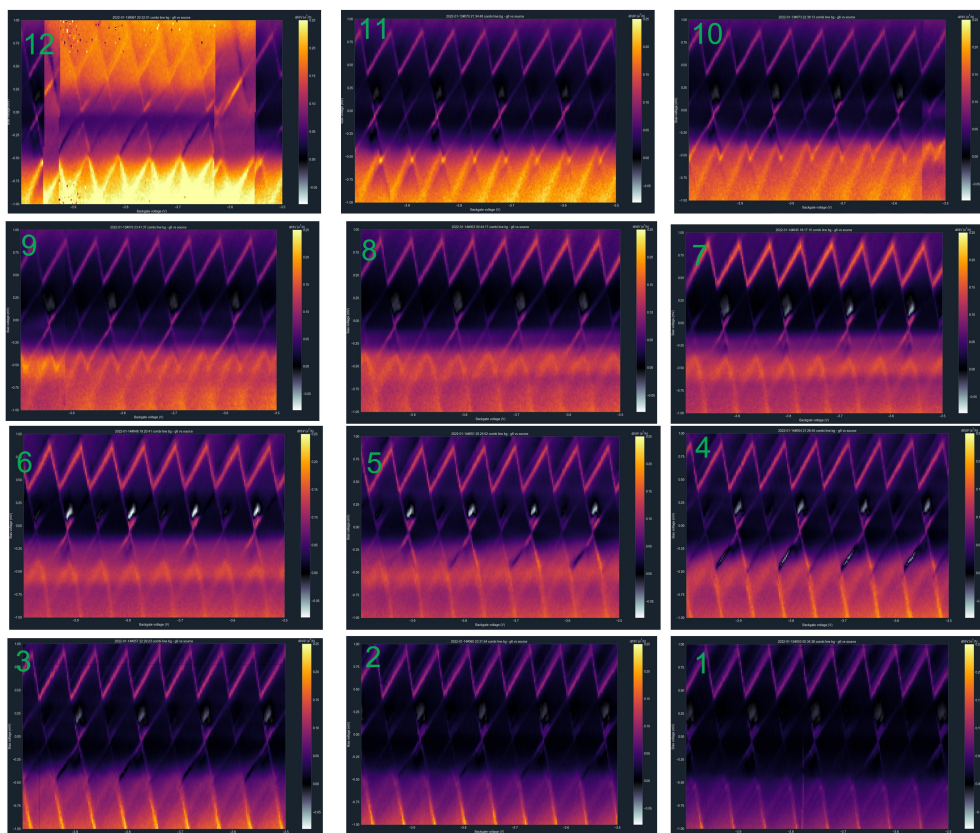# Appandix E: Coulomb diamonds across QD resonance at 0.17 T

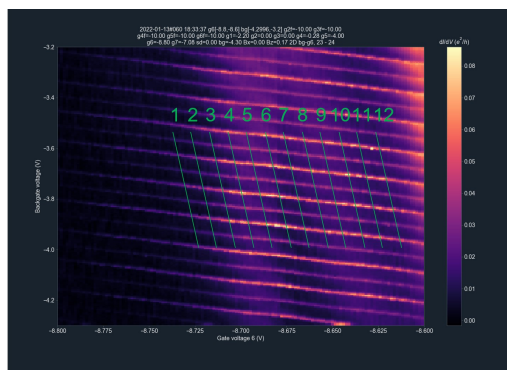Figure 33: Same as fig.32 but at a set magnetic field.
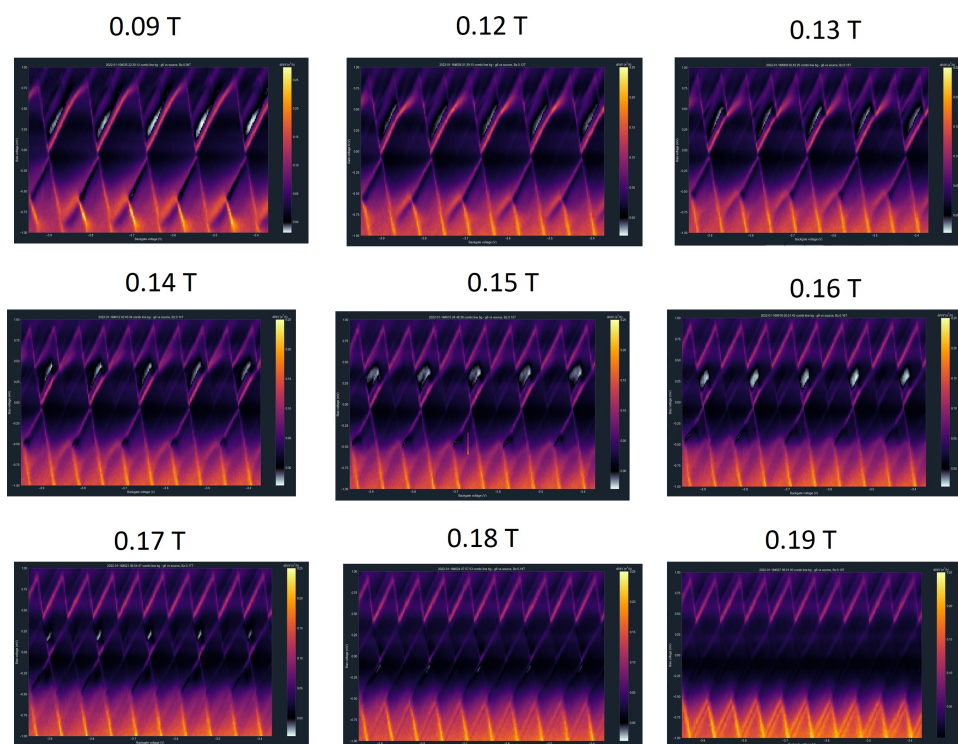
Appandix F: Coulomb diamond in steps of magnetic field

Figure 34: Coulomb diamonds in steps of magnetic field in medium coupled region. The quaziparticle poisoning appears with $B_{||}$.

References

1. Xin, S. *et al.* Solid-state lithium metal batteries promoted by nanotechnology: progress and prospects. *ACS Energy Letters* **2,** 1385–1394 (2017).

2. Sahu, T. *et al.* Nanotechnology based drug delivery system: Current strategies and emerging therapeutic potential for medical science. *Journal of Drug Delivery Science and Technology* **63,** 102487 (2021).

3. Mikolajick, T., Heinzig, A., Trommer, J., Baldauf, T. & Weber, W. The RFET—A reconfigurable nanowire transistor and its application to novel electronic circuits and systems. *Semiconductor Science and Technology* **32,** 043001 (2017).

4. Mokkapati, S. & Jagadish, C. Review on photonic properties of nanowires for photovoltaics. *Optics express* **24,** 17345–17358 (2016).

5. Caballero-Calero, O. & Martín-González, M. Thermoelectric nanowires: A brief prospective. *Scripta materialia* **111,** 54–57 (2016).

6. Ihn, T. *Semiconductor Nanostructures: Quantum states and electronic transport* (OUP Oxford, 2009).

7. Liang, D., Du, J. & Gao, X. P. InAs nanowire devices with strong gate tunability: fundamental electron transport properties and application prospects: a review. *Journal of Materials Science & Technology* **31,** 542–555 (2015).

8. Lutchyn, R. M. *et al.* Majorana zero modes in superconductor–semiconductor heterostructures. *Nature Reviews Materials* **3,** 52–68 (2018).

9. Winkler, G. W., Wu, Q., Troyer, M., Krogstrup, P. & Soluyanov, A. A. Topological phases in InAs 1- x Sb x: from novel topological semimetal to Majorana wire. *Physical Review Letters* **117,** 076403 (2016).

10. Deng, M. *et al.* Majorana bound state in a coupled quantum-dot hybrid-nanowire system. *Science* **354,** 1557–1562 (2016).

11. Chevallier, D., Szumniak, P., Hoffman, S., Loss, D. & Klinovaja, J. Topological phase detection in Rashba nanowires with a quantum dot. *Physical Review B* **97,** 045404 (2018).

12. Baba, S. *et al.* Cooper-pair splitting in two parallel InAs nanowires. *New Journal of Physics* **20,** 063021 (2018).

13. Leng, Y. *Materials characterization: introduction to microscopic and spectroscopic methods* (John Wiley & Sons, 2009).

14. CARTER, B. A., Williams, D. B., Carter, C. B. & Williams, D. B. *Transmission electron microscopy: a textbook for materials science. Diffraction. II* (Springer Science & Business Media, 2009).

15. Madsen, M. H. *et al.* Experimental determination of adatom diffusion lengths for growth of InAs nanowires. *Journal of crystal growth* **364,** 16–22 (2013).

16. Xu, T. *et al.* Faceting, composition and crystal phase evolution in III–V antimonide nanowire heterostructures revealed by combining microscopy techniques. *Nanotechnology* **23,** 095702 (2012).

17. Davidson, F. M., Lee, D. C., Fanfair, D. D. & Korgel, B. A. Lamellar twinning in semiconductor nanowires. *The Journal of Physical Chemistry C* **111,** 2929–2935 (2007).

18. Schnedler, M. *et al.* Composition modulation by twinning in InAsSb nanowires. *Nanotechnology* **30,** 324005 (2019).

19. Belabbes, A., Panse, C., Furthmüller, J. & Bechstedt, F. Electronic bands of III-V semiconductor polytypes and their alignment. *Physical Review B* **86,** 075208 (2012).

20. Thelander, C., Caroff, P., Plissard, S., Dey, A. W. & Dick, K. A. Effects of crystal phase mixing on the electrical properties of InAs nanowires. *Nano letters* **11,** 2424–2429 (2011).

21. Nilsson, M. *et al.* Single-electron transport in InAs nanowire quantum dots formed by crystal phase engineering. *Physical Review B* **93,** 195422 (2016).

22. Dick, K. A. *et al.* Parameter space mapping of InAs nanowire crystal structure. *Journal of Vacuum Science & Technology B, Nanotechnology and Microelectronics: Materials, Processing, Measurement, and Phenomena* **29,** 04D103 (2011).

23. Probst, C. E., Zrazhevskiy, P., Bagalkot, V. & Gao, X. Quantum dots as a platform for nanoparticle drug delivery vehicle design. *Advanced drug delivery reviews* **65,** 703–718 (2013).

24. Berer, T. *et al.* Lateral quantum dots in Si/ Si Ge realized by a Schottky split-gate technique. *Applied Physics Letters* **88,** 162112 (2006).

25. Björk, M. T. *et al.* Few-electron quantum dots in nanowires. *Nano Letters* **4,** 1621–1625 (2004).

26. Thelander, C. *et al.* Single-electron transistors in heterostructure nanowires. *Applied Physics Letters* **83,** 2052–2054 (2003).

27. Mattox, D. M. *Handbook of physical vapor deposition (PVD) processing* (William Andrew, 2010).

28. Sestoft, J. E. *et al.* Engineering hybrid epitaxial InAsSb/Al nanowires for stronger topological protection. *Physical Review Materials* **2,** 044202 (2018).

29. Degtyarev, V., Khazanova, S. & Demarina, N. Features of electron gas in InAs nanowires imposed by interplay between nanowire geometry, doping and surface states. *Scientific reports* **7,** 1–9 (2017).

30. Li, T. *et al.* Improving the electrical properties of InAs nanowire field effect transistors by covering them with Y 2 O 3/HfO 2 layers. *Nanoscale* **10,** 18492–18501 (2018).

31. Thelander, C., Caroff, P., Plissard, S. & Dick, K. A. Electrical properties of InAs1- xSbx and InSb nanowires grown by molecular beam epitaxy. *Applied Physics Letters* **100,** 232105 (2012).

32. Boland, J. L. *et al.* High electron mobility and insights into temperature-dependent scattering mechanisms in InAsSb nanowires. *Nano letters* **18,** 3703–3710 (2018).

33. Kanne, T. *et al.* Epitaxial Pb on InAs nanowires for quantum devices. *Nature Nanotechnology* **16,** 776–781 (2021).

34. Zhang, H., Liu, D. E., Wimmer, M. & Kouwenhoven, L. P. Next steps of quantum transport in Majorana nanowire devices. *Nature communications* **10,** 1–7 (2019).

35. Annett, J. F. *et al. Superconductivity, superfluids and condensates* (Oxford University Press, 2004).

36. Swihart, J., Scalapino, D. & Wada, Y. Solution of the gap equation for Pb, Hg, and Al. *Physical Review Letters* **14,** 106 (1965).

37. Coleman, P. *Introduction to many-body physics* (Cambridge University Press, 2015).

38. Sauls, J. *Andreev bound states and their signatures* 2018.

39. Krizek, F. *et al.* Growth of InAs wurtzite nanocrosses from hexagonal and cubic basis. *Nano letters* **17,** 6090–6096 (2017).

40. Wang, F. *et al.* Surface roughness induced electron mobility degradation in InAs nanowires. *Nanotechnology* **24,** 375202 (2013).

41. Albrecht, S. *et al.* Transport signatures of quasiparticle poisoning in a Majorana island. *Physical review letters* **118,** 137701 (2017).

42. Ménard, G. C. *et al.* Suppressing quasiparticle poisoning with a voltage-controlled filter. *Physical Review B* **100,** 165307 (2019).

43. Shen, J. *et al.* Parity transitions in the superconducting ground state of hybrid InSb–Al Coulomb islands. *Nature communications* **9,** 1–8 (2018).

44. Albrecht, S. M. *et al.* Exponential protection of zero modes in Majorana islands. *Nature* **531,** 206–209 (2016).

45. Lai, Y.-H., Sarma, S. D. & Sau, J. D. Theory of Coulomb blockaded transport in realistic Majorana nanowires. *Physical Review B* **104,** 085403 (2021).

46. Jünger, C. H. *Transport spectroscopy of semiconductor superconductor nanowire hybrid devices* PhD thesis (University_of_Basel, 2019).

47. Gramich, J., Baumgartner, A. & Schönenberger, C. Resonant and inelastic Andreev tunneling observed on a carbon nanotube quantum dot. *Physical review letters* **115,** 216801 (2015).

48. Vaitiekėnas, S., Deng, M.-T., Nygård, J., Krogstrup, P. & Marcus, C. Effective g factor of subgap states in hybrid nanowires. *Physical review letters* **121,** 037703 (2018).

49. Konopka, J. Conduction electron spin resonance in InAs. *Physics Letters A* **26,** 29–31 (1967).

50. Rainis, D. & Loss, D. Majorana qubit decoherence by quasiparticle poisoning. *Physical Review B* **85,** 174533 (2012).